RSC Advances

ROYAL SOCIETY OF CHEMISTRY

PAPER

View Article Online
View Journal | View Issue

Cite this: *RSC Adv.*, 2026, **16**, 21168

Lead-free new alkali metals double perovskites A_2InAgF_6 (A = Na, K, and Rb) for optoelectronic applications: a first-principles study

Sharmin Islam, [a] Shatha A. Aldaghfag, [b] Ali El-Rayyes, [c] Abdullah Al Mahmud, [a] Samah Saidi, [d] Omar Alsalmi, [e] Mohd Taukeer Khan *[f] and Md Saiduzzaman *[a]

Received 16th February 2026
Accepted 9th April 2026

DOI: 10.1039/d6ra01318j

rsc.li/rsc-advances

The growing demand for sustainable energy and the environmental drawbacks of lead-based perovskites have led to the emergence of lead-free double perovskites as promising alternatives. In this work, first-principles calculations based on density functional theory (DFT) are employed to systematically investigate the structural, mechanical, electronic, optical, and thermodynamic properties of fluoride-based double perovskites A_2InAgF_6 (A = Na, K, and Rb). Structural analysis confirms that all three compounds are stable in the cubic space group, with negative formation energies. Mechanical evaluations demonstrate that all three compounds satisfy the Born-stability criteria and exhibit ductile behavior. Electronic band structure calculations reveal that these materials are direct bandgap semiconductors, with bandgaps increasing from 3.02 eV for Na_2InAgF_6 to 3.88 eV for Rb_2InAgF_6 using the Hybrid-HSE06 functional. Furthermore, the materials exhibit low reflectivity and strong optical absorption in the UV range, alongside stable thermodynamic profiles at high temperature. These findings highlight the potential of A_2InAgF_6 compounds for next-generation optoelectronic, photovoltaic, and thermoelectric applications.

1 Introduction

The increasing depletion of fossil fuels and the urgent need to reduce carbon emissions have made solar energy a promising renewable solution to the global energy crisis.[1,2] The efficiency of solar cells depends on the optical and electronic properties of the materials used.[3] Although silicon-based photovoltaic cells dominate the market due to their reliability and efficiency, their broader use is restricted by high production costs and modest power conversion efficiency (PCE).[4,5] Perovskites have attracted significant attention as promising alternatives for emerging solar cell technologies. Since 2009, perovskite solar cells have achieved PCEs exceeding 25%, comparable to commercial silicon-based cells.[6] This performance arises from their unique properties, including long charge-carrier diffusion lengths, tunable bandgaps, and low exciton binding energies.[7,8] These features enable applications in solar cells, light emitting diodes, photodetectors, and thermoelectric devices.[8,9] Additionally, they are low cost, lightweight, and amenable to large-scale fabrication.[10] However, conventional Pb-based perovskites suffer from serious drawbacks such as toxicity and poor stability under moisture, heat, and UV exposure,[11] motivating the exploration of lead-free alternatives such as double perovskites.[12]

The $A_2BB'X_6$ double perovskite structure has recently gained attention for sustainable energy applications due to its compositional flexibility and ecofriendly nature. These materials crystallize in the cubic $Fm\bar{3}m$ structure, where the A-site is occupied by alkali metal ions (*e.g.*, K^+, Rb^+); the B and B′ sites by mono- and trivalent cations (*e.g.*, Ag^+, Cu^+, In^{3+}, Bi^{3+}), and the X-site by halogens (*e.g.*, F^-, Cl^-, Br^-, I^-).[13,14] This structural versatility allows tuning of bandgaps, carrier mobility, and optical absorption, making them suitable for photovoltaic and optoelectronic applications. Lead-free double perovskites such as $Cs_2AgBiBr_6$ and $Cs_2AgBiCl_6$ show indirect and large bandgaps (>2 eV), limiting efficiency, while Cs_2TiBr_6 exhibits an improved bandgap and a power conversion efficiency (PCE) of 3.3%.[15,16] To overcome such limitations, halide substitution and cation engineering have been widely used to tune material properties. These materials exhibit good stability, long carrier diffusion lengths, and strong optical absorption, making them promising for optoelectronic applications.[17,18]

[a]*Department of Materials Science and Engineering, Khulna University of Engineering & Technology, Khulna 9203, Bangladesh. E-mail: msaiduzzaman@mse.kuet.ac.bd*

[b]*Department of Physics, College of Sciences, Princess Nourah bint Abdulrahman University, P. O. Box 84428, Riyadh 11671, Saudi Arabia*

[c]*Center for Scientific Research and Entrepreneurship, Northern Border University, 73213, Arar, Saudi Arabia*

[d]*Department of Physics, College of Science and Humanities in Al-Kharj, Prince Sattam Bin Abdulaziz University, Al-Kharj 11942, Saudi Arabia*

[e]*Department of Physics, College of Science, Umm Al-Qura University, Makkah, 21955, Saudi Arabia*

[f]*Department of Physics, Faculty of Science, Islamic University of Madinah, Madinah, Saudi Arabia. E-mail: khanmtk@iu.edu.sa*

Recent studies further demonstrate the potential of Pb-free double perovskites. For example, A_2YAuI_6 (A = Rb, Cs), studied by Nazir *et al.*,[19] shows ductile behavior and direct bandgaps (~1.7 eV) suitable for clean energy. X_2AgBiI_6 (X = K, Rb, Cs) exhibits stability, ideal bandgaps (1.26–1.35 eV), strong absorption, and promising thermoelectric performance.[20] Nasir *et al.*[21] reported X_2CuAsF_6 (X = Na, K) with bandgaps (0.8 to 1.56 eV) and strong optical response.[21] $A_2AlAuCl_6$ (A = Cs, K, Rb) shows ~2 eV bandgaps with UV-visible absorption and thermoelectric potential.[22] A-site substitution significantly influences properties; for example, A_2AgAlI_6 (A = Na, K, and Rb) demonstrates decreasing bandgaps with A-site variation,[23] while $Rb_2AlAgCl_6$ and $Cs_2AlAgCl_6$ studied by Lantri *et al.*[24] reveal bandgap tuning and UV responsiveness. Similarly, K_2AlInI_6, Rb_2AlInI_6, & Cs_2AlInI_6 highlight the A site effect on electronic and thermoelectric properties.[25] Studies on K_2NaInX_6 (ref. 26) and Rb_2GeSnX_6 reveal halide-dependent tuning of optical and thermoelectric properties.[27] Recent first-principles studies on Rb_2NaTlZ_6 (Z = Cl, Br, I) by Shah *et al.*[28] report structural stability, direct bandgaps (3.4–2.1 eV), and thermoelectric performance (*ZT* up to 0.71). DFT studies on Cs_2NaXCl_6 (X = In, La, Sc, Y) by Shakeel *et al.*[29] show stability, wide bandgaps (4.1–6.4 eV), strong UV absorption, and low thermal conductivity (0.169–0.228 W mK^{-1}). Rb_2CuSbX_6 (X = Cl, Br, I) exhibits pressure-dependent bandgaps (1.08–0.33 eV) and tunable optoelectronic and thermoelectric properties.[30] In another study by Shah *et al.*,[31] K_2NaTIX_6 (X = Cl, Br, I) exhibits strain-tunable direct bandgaps and improved optoelectronic properties under uniaxial strain (−4% to 4%). Saeed *et al.*[32] reported that X_2BAgCl_6 (X = K, Rb, Cs; B = Sc, Y) exhibits semiconducting behaviour with bandgaps (3.56–4.88 eV), strong UV absorption, and moderate thermoelectric performance ($ZT \approx 0.38$–0.42).

Despite these advances, fluoride-based double perovskites remain less explored than iodide, bromide, and chloride systems. In particular, a systematic theoretical study of A-site cation effects on structural stability and optoelectronic properties is still lacking, representing an important scientific gap. In this context, A_2InAgF_6 (A = Na, K, and Rb) provides an ideal platform to investigate the role of A-site cation size and chemistry. These compounds consist of non-toxic elements and are promising for sustainable applications, while Ag^+ and In^{3+} are expected to enhance structural stability and electronic performance. Therefore, in this work, density functional theory (DFT) is employed to study the structural, electronic, optical, phonon, and thermodynamic properties of A_2InAgF_6 (A = Na, K, and Rb). The objective of this work is to understand the effect of A-site variation and identify the most suitable composition for efficient and stable clean energy applications.

2 Computational methods

First-principles calculations based on DFT[33,34] were performed using the Cambridge Serial Total Energy Package (CASTEP) module.[35] The electronic exchange–correlation interactions were treated using the generalized gradient approximation (GGA) with the Perdew–Burke–Ernzerhof (PBE)[36] functional for geometry optimization and electronic properties calculation. Additionally, spin–orbit coupling (SOC) was incorporated. For more precise evaluation of the bandgaps and optical properties, the Hybrid-HSE06 functional was employed in the calculations. Ultrasoft pseudopotentials were employed to describe the core-valence electron interactions for all elements. The structural optimization of the crystal was conducted using the Broyden–Fletcher–Goldfarb–Shanno (BFGS) minimization scheme.[37–40] The plane-wave basis set energy cutoff was set to 500 eV, and a Monkhorst–Pack *k*-point mesh of 4 × 4 × 4 was used to sample the Brillouin zone.[41,42] The convergence thresholds were set to 1.0×10^{-6} eV per atom for self-consistent field (SCF) cycles, and 1.0×10^{-5} eV per atom for total energy. Additionally, the maximum force, stress, and atomic displacement tolerances were set to 0.03 eV $Å^{-1}$, 0.05 GPa, and 0.001 Å, respectively. A *k*-point mesh of 8 × 8 × 8 was chosen, and the Kramers–Kronig relations were used to derive the frequency-dependent complex dielectric function, which allowed optical constants, including the absorption coefficient, refractive index, and reflectivity, to be calculated.[43] Small finite strains were applied to the optimized structure in order to evaluate the second-order elastic constants. The GGA-PBEsol framework, which offers better lattice parameter predictions for solids, was used for these computations. The determined elastic constants were used to investigate mechanical stability and anisotropy. The final crystal structures of A_2InAgF_6 fluoride perovskites are visualized using the VESTA visualization software.[44] The elastic modulus parameters are produced using three-dimensional rendering by means of the ELATE software.[45] Phonon dispersion and thermodynamic calculations were performed using a higher cutoff energy of 880 eV and a reduced 2 × 2 ×2 *k*-point grid to ensure the accuracy of the lattice dynamical properties.[41] The convergence criteria for these calculations were set to 0.5×10^{-5} eV per atom for SCF energy, 0.1×10^{-1} eV $Å^{-1}$ for force, 0.2×10^{-1} GPa for stress, and 0.5×10^{-3} Å for displacement.

3 Result and discussions

3.1 Structural properties

The cubic space group $Fm\bar{3}m$ (# 225) represents the fundamental crystal symmetry of double perovskites with the general formula $A_2B'B''X_6$.[15] The fluoride double perovskites A_2InAgF_6 (A = Na, K, and Rb) also crystallize in this highly symmetric cubic structure, which is characteristic of stable double perovskite systems. Each conventional unit cell contains 40 atoms, corresponding to four formula units. The alkali metal cations (Na^+, K^+, and Rb^+) are accommodated within the interstitial sites of the perovskite lattice, where they play a crucial role in stabilizing the overall crystal structure. Fig. 1 presents the schematic crystal structure of the cubic double perovskite A_2InAgF_6. In this structure, the alkali metal cations occupy the 8c Wyckoff positions (0.25, 0.25, 0.25), while the In^{3+} ions are located at the 4a sites (0, 0, 0) and the Ag^+ ions reside at the 4b sites (0, 0, 0.5). The fluoride anions are positioned at the 24e sites (0, 0, *x*), where the internal coordinate *x* shows a slight dependence on the size of the A-site cation.

The formation enthalpy values are computed using the following equation:

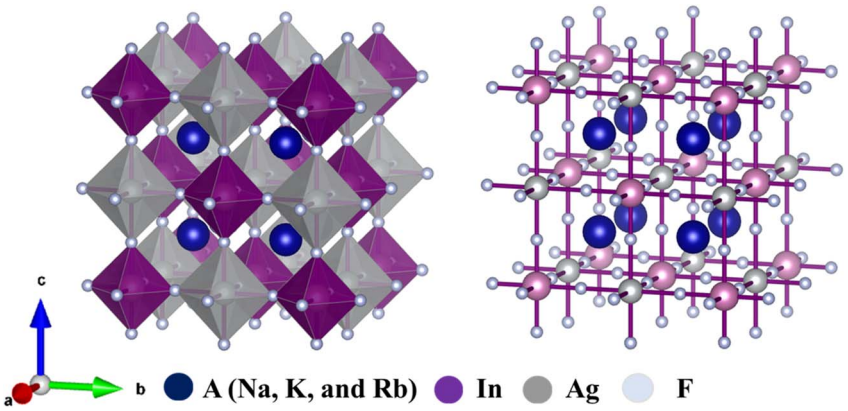

Fig. 1 The schematic crystal representation of the double perovskite A_2InAgF_6 (A = Na, K, and Rb) structure.

$$\Delta E_f = \frac{1}{N}\left[E_{A_2InAgF_6} - 2E_A^{bulk} - E_{In}^{bulk} - E_{Ag}^{bulk} - 3E_{F_2}\right] \quad (1)$$

The formation energy ΔE_f represents the energy change associated with forming the compound A_2InAgF_6 from its constituent elements in their most stable bulk and molecular reference states. In this expression, $E_{A_2InAgF_6}$ denotes the total energy of the optimized compound obtained from DFT calculations. The terms E_A^{bulk}, E_{In}^{bulk}, and E_{Ag}^{bulk} correspond to the energies per atom of the alkali metal (A = Na, K, Rb), indium, and silver in their respective bulk crystalline phases. The fluorine contribution is represented by E_{F_2}, which is the total energy of an isolated fluorine molecule, and it is multiplied by 3 because six fluorine atoms in the compound correspond to three F_2 molecules. The factor $\frac{1}{N}$ normalizes the total energy difference per atom, where N is the total number of atoms in the formula unit (10 in this case). A negative value of ΔE_f indicates that the compound is thermodynamically stable with respect to its elemental constituents. The calculated formation energies (ΔE_f) are negative for all three compounds, confirming their stability and spontaneous formation tendency from their constituent elements.[46] Among the studied systems, Rb_2InAgF_6 exhibits the most negative formation energy (−2.319 eV per atom), indicating the highest structural stability as shown in Fig. 2(a). In comparison, K_2InAgF_6 shows a slightly less negative value (−2.298 eV per atom), while Na_2InAgF_6 has the least negative formation energy (−2.114 eV per atom), suggesting comparatively lower lattice cohesion. The increase in stability with increasing A-site ionic size can be attributed to enhanced lattice strain and reduced geometric compatibility within the perovskite framework. Additionally, we also calculated cohesive and binding energy. The following equations are used to calculate the cohesive and binding energy:

$$\Delta E_c = \frac{1}{N}\left[E_{A_2InAgF_6} - 2E_A^{iso} - E_{In}^{iso} - E_{Ag}^{iso} - 6E_F^{iso}\right] \quad (2)$$

$$\Delta E_b = \frac{1}{N}\left[2E_A^{iso} + E_{In}^{iso} + E_{Ag}^{iso} + 6E_F^{iso} - E_{A_2InAgF_6}\right] \quad (3)$$

The cohesive energy ΔE_c and binding energy ΔE_b describe the strength of atomic bonding in A_2InAgF_6, but they are defined with slightly different sign conventions. In the cohesive energy expression, $E_{A_2InAgF_6}$ is the total energy of the compound, while E_A^{iso}, E_{In}^{iso}, E_{Ag}^{iso}, and E_F^{iso} represent the energies of isolated (free) atoms of A, In, Ag, and F, respectively. These isolated atomic energies are multiplied by their stoichiometric coefficients (2 for A, 1 for In, 1 for Ag, and 6 for F) to account for all atoms in the formula unit. The cohesive energy equation calculates the energy difference between the compound and its constituent isolated atoms, normalized by the total number of atoms N, and typically yields a negative value, indicating energy release upon formation of the solid from free atoms. In contrast, the binding energy ΔE_b uses the same terms but reverses the subtraction order, effectively measuring the energy required to break the compound into isolated atoms. As

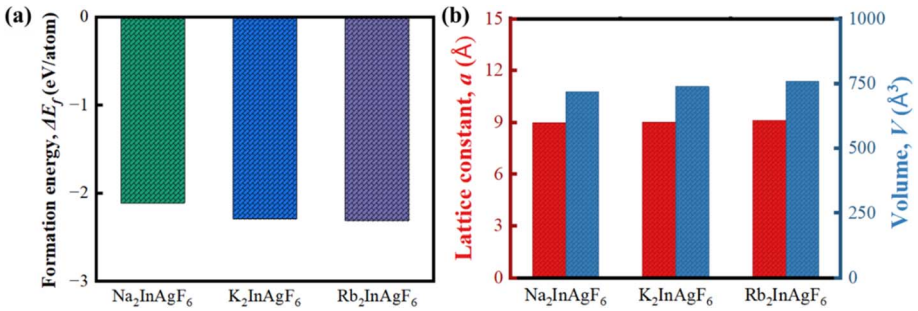

Fig. 2 (a) Formation energy, (b) lattice constant, and volume for A_2InAgF_6 (A = Na, K, and Rb) compounds.

a result, binding energy is usually positive for stable systems. Both quantities provide insight into bond strength and structural stability, with larger magnitudes indicating stronger interatomic interactions. The calculated cohesive energies of Na_2InAgF_6, K_2InAgF_6, and Rb_2InAgF_6 are −4.154, −4.231, and −4.226 eV per atom, respectively. This decrease in cohesive energy indicates a weakening of the internal bonding strength, as a lower amount of energy is required to separate the crystal into its constituent isolated atoms. Similarly, the calculated binding energies for Na_2InAgF_6, K_2InAgF_6, and Rb_2InAgF_6 are also found to be 4.154, 4.231, and 4.226 eV per atom, respectively. This well-ordered atomic arrangement gives rise to a highly symmetric cubic lattice and ensures ideal octahedral coordination around the B-site metal ions. The increase in ionic size leads to an expansion of the perovskite lattice, resulting in an increase in the lattice constant from 8.98 Å for Na_2InAgF_6 to 9.05 Å for K_2InAgF_6 and further to 9.12 Å for Rb_2InAgF_6 as shown in Fig. 2(b). The unit cell volume increases from 720.44 $Å^3$ to 740.15 $Å^3$ and 760.09 $Å^3$, respectively. This behavior is consistent with the fundamental characteristics of perovskite structures, where larger A-site cations enlarge the perovskite cage by increasing the metal–fluorine bond lengths and inter-octahedral spacing.[49] Laihnuna *et al.* reported the lattice parameter and formation energy of K_2InAgF_6, while Laihnuna *et al.* and Ahmad *et al.* reported comparable structural and energetic parameters for $K_2InAgCl_6$, $K_2InAgBr_6$, and K_2InAgI_6; these values are in good agreement with our results, confirming the reliability of the present calculations.[47,48] All the values are given in Table 1.

The structural stability was further assessed using the Goldschmidt tolerance factor (τ_G), and the octahedral factor (μ) defined as:

$$\tau_G = \frac{r_A + r_X}{\sqrt{2}\left(\left(\frac{r_B + r_{B'}}{2}\right) + r_X\right)} \quad (4)$$

$$\mu = \frac{\left(r_B + r_{B'}\right)}{2r_X} \quad (5)$$

where r_A, r_B, $r_{B'}$ and r_X stand for the elements' respective Shannon ionic radii at locations A, B, B′, and X. Table 2 demonstrates the ionic radius of each atom. For stable cubic perovskites, the tolerance factor typically lies within the range $0.825 < \tau_G < 1.059$, while the octahedral factor satisfies $0.414 < \mu < 0.732$.[50] The calculated values for A_2InAgF_6 (A = Na, K, and Rb), presented in Table 3, fall within these acceptable limits, confirming their structural compatibility with the cubic perovskite framework. The tolerance factors are 0.83 for Na_2InAgF_6, 0.91 for K_2InAgF_6, and 0.94 for Rb_2InAgF_6. The closer proximity of τ_G to unity for K_2InAgF_6 and Rb_2InAgF_6 indicates a more favorable cubic perovskite geometry, whereas the lower value for Na_2InAgF_6 suggests increased octahedral distortion due to size mismatch at the A-site. This confirms that larger alkali ions provide better structural stabilization of the cubic framework.[51]

Bartel *et al.*[52] proposed another tolerance factor to predict the stability of perovskite materials. To further assess structural stability, the data driven tolerance factor proposed by Bartel *et al.* was used, given by:

$$\tau_B = \frac{r_X}{\left(\frac{r_B + r_{B'}}{2}\right)} - n_A\left(n_A - \frac{\frac{r_A}{\left(\frac{r_B + r_{B'}}{2}\right)}}{\ln\left(\frac{r_A}{\left(\frac{r_B + r_{B'}}{2}\right)}\right)}\right) \quad (6)$$

Table 2 Shannon ionic radii of constituent ions in A_2InAgF_6 (A = Na, K, and Rb)

Ion	Ionic radius (Å) [Shannon ionic radii (1976)]
Na^+ (12-coordinated)	1.39
K^+ (12-coordinated)	1.64
Rb^+ (12-coordinated)	1.72
In^{3+} (6-coordinated)	0.80
Ag^+ (6-coordinated)	1.15
F^- (6-coordinated)	1.33

Table 3 Goldschmidt's tolerance factor (τ_G), Bartel's tolerance factor (τ_B) and octahedral factor (μ) for A_2InAgF_6 (A = Na, K, and Rb) compounds

Compound	τ_G	τ_B	μ
Na_2InAgF_6	0.83	4.384	0.73
K_2InAgF_6	0.91	3.599	0.73
Rb_2InAgF_6	0.94	3.472	0.73

Table 1 Calculated lattice constants *a* (Å), unit cell volume *V* ($Å^3$), formation energy (ΔE_f), cohesive energy (ΔE_c), and binding energy (ΔE_b)

Compound	Lattice parameter, *a* (Å)		*V* ($Å^3$)	Formation energy, (eV per atom)	Cohesive energy, (eV per atom)	Binding energy, (eV per atom)
	This study	Previous study				
Na_2InAgF_6	8.98	—	720.44	−2.114	−4.154	4.154
K_2InAgF_6	9.05	9.003 (ref. 47)	740.15	−2.298	−4.231	4.231
Rb_2InAgF_6	9.12	—	760.09	−2.319	−4.226	4.226
$K_2InAgCl_6$ (ref. 47 and 48)	—	10.502, 19.930	—	—	—	—
$K_2InAgBr_6$ (ref. 47 and 48)	—	11.0543, 20.9559	—	—	—	—
K_2InAgI_6 (ref. 47 and 48)	—	11.8904, 22.5263	—	—	—	—

where n_A is the oxidation state of the A-site cation. According to this criterion, double perovskites are structurally stable when $\tau_B < 4.63$.[52] The calculated values (3.599 for K, 3.472 for Rb, and 4.384 for Na) confirm that all three compounds fall within the stability range. However, the relatively higher τ_B value of Na_2InAgF_6 indicates greater lattice strain, while K_2InAgF_6 and Rb_2InAgF_6 exhibit superior geometric compatibility and structural robustness. Therefore, the calculated τ_B values, presented in Table 3, further support the structural stability of the studied compounds.

Overall, the combined analysis of lattice parameters, formation energy, and tolerance factors demonstrates that K_2InAgF_6 and Rb_2InAgF_6 possess highly stable cubic double perovskite structures, whereas Na_2InAgF_6, although stable, shows comparatively higher structural distortion. This systematic dependence of structural stability on the A-site cation size plays a crucial role in tuning the mechanical, vibrational, and optoelectronic properties of fluoride double perovskites.

3.2 Mechanical properties

In density functional theory, the reaction of a material to stress and other conditions is described in terms of its mechanical properties.[53] The elastic stiffness constants symbolized by the C_{ij} matrix in Table 4 describe the mechanical response of Na_2InAgF_6, K_2InAgF_6, and Rb_2InAgF_6 and illustrated in Fig. 3(a). These constants are also significant for their structural stability, anisotropy, and potential applications.

The elastic constant C_{11} defines how a material resists forces of compression along the principal crystallographic direction. Measurement of elasticity creates higher stiffness along this particular direction.[54] C_{12} measurements define the behavior of the material to respond to stress that is equally acting on multiple axes, stress is applied in one direction, and strain in a direction perpendicular [1 1 0] plane.[55] The material responds to shear strains through the Shear Elastic Constant measurement expressed as C_{44}. The concept of resistance to the change in shape without a change in volume is an important aspect to explore.[56] The Born stability criteria of the compounds are described through the equations noted below:[57]

$$C_{11} > 0,\ C_{44} > 0,\ C_{11}-C_{12} > 0,\ C_{11} + 2C_{12} > 0 \quad (7)$$

Among the three compounds, Na_2InAgF_6 has the highest C_{11} value at 63.69 GPa. This means it resists uniaxial stress better than K_2InAgF_6 (60.26 GPa) and Rb_2InAgF_6 (50.65 GPa). The higher resistance of Na_2InAgF_6 comes from the shorter and stronger In–F bonds, which give improved strength along the axis. For C_{12}, Na_2InAgF_6 has the largest value of 26.06 GPa, while Rb_2InAgF_6 shows 23.80 GPa, and K_2InAgF_6 has 23.50 GPa. Na_2InAgF_6 exhibits more resistance to uniform multidirectional stress compared to the other two compounds. For shear resistance, the C_{44} values show that Rb_2InAgF_6 (10.72 GPa) has the strongest one. Na_2InAgF_6 and K_2InAgF_6 have the C_{44} values of 6.22 GPa and 7.07 GPa, respectively. As a conclusion, Rb_2InAgF_6 resists shape changes better than the others. Therefore, Na_2InAgF_6 has the highest resistance to compression, but Rb_2InAgF_6 is stronger against shear deformations. These compounds show moderate stiffness and elastic anisotropy, which makes them suitable for mechanical and optoelectronic applications.[58] Cauchy pressure (C_p) is an indicator of whether a material is ductile or brittle. Negative values signify brittleness, while positive values suggest ductility.[59] The parameter known as crystal stiffness (C_s) measures the overall rigidity of the crystal structure.[60]

A material's ability to resist changes in shape reflects its mechanical strength, as these characteristics are directly linked to its level of robustness. The Kleinman parameter (ζ) describes how easily the internal coordinates of a crystal can be modified when subjected to an applied strain. The formulas for determining Cauchy pressure, crystal stiffness, and the Kleinman parameter are as follows:

$$C_p = C_{12} - C_{44} \quad (8)$$

$$C_s = \frac{C_{11} - C_{12}}{2} \quad (9)$$

$$\zeta = \frac{C_{11} + 8C_{12}}{7C_{11} + 2C_{12}} \quad (10)$$

The C_p of Na_2InAgF_6 is 19.83 GPa, which is the highest among the compounds. This shows that it is the most ductile, compared to K_2InAgF_6 (16.43 GPa) and Rb_2InAgF_6 (13.08 GPa). The higher ductility of Na_2InAgF_6 can be explained by the stronger bonding created by the smaller Na^+ ion, which improves structural integrity and resistance to brittle failure. The crystal stiffness (C_s) values are 18.82 GPa for Na_2InAgF_6, 18.38 GPa for K_2InAgF_6, and 13.42 GPa for Rb_2InAgF_6. Na_2InAgF_6 shows the highest crystal stiffness parameter (C_s), indicating stronger resistance to lattice deformation at the atomic scale. The reason is that the Na–F bonds are shorter and stronger than K–F and Rb–F bonds, as the ionic radius of Na^+ is smaller, leading to stronger electrostatic attraction. For the Kleinman parameter (ζ), Rb_2InAgF_6 has the highest value at 0.60. Na_2InAgF_6 has the value at 0.55, and K_2InAgF_6 has the lowest value at 0.53. This means Rb_2InAgF_6 is the most flexible among the three compounds. The larger size of Rb^+ weakens the bonding strength, which makes the lattice more adaptable to internal distortions under stress. Na_2InAgF_6 offers the best balance between ductility and thermal stability. Rb_2InAgF_6 exhibits higher stiffness and lower anisotropy, making each compound suitable for different mechanical applications. However, its lower bulk modulus and melting temperature

Table 4 Calculated elastic stiffness constants for Na_2InAgF_6, K_2InAgF_6, and Rb_2InAgF_6

Compounds	C_{11}	C_{12}	C_{44}	C_s	C_p	ζ
Na_2InAgF_6	63.69	26.06	6.22	18.82	19.83	0.55
K_2InAgF_6	60.26	23.50	7.07	18.38	16.43	0.53
Rb_2InAgF_6	50.65	23.80	10.72	13.42	13.08	0.60
$K_2InAgCl_6$ (ref. 48)	44.42	22.82	7.31	—	15.51	—
$K_2InAgBr_6$ (ref. 48)	47.43	14.86	9.81	—	5.05	—
K_2InAgI_6 (ref. 48)	43.17	8.59	8.24	—	0.36	—

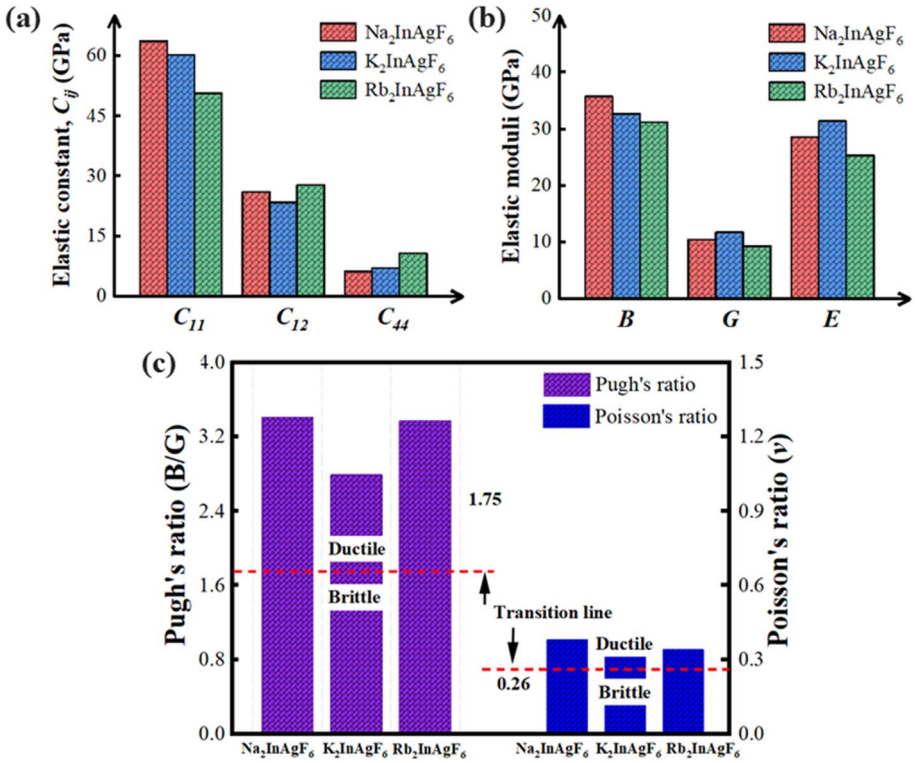

Fig. 3 The comparison of the A_2InAgF_6 (A = Na, K, and Rb) compounds' (a) elastic constants C_{ij}, (b) elastic moduli, and (c) Pugh's ratio & Poisson's ratio.

suggest reduced resistance to volumetric compression and lower thermal stability compared to Na_2InAgF_6. Material's resistance to volumetric deformation under applied pressure is measured by its bulk modulus (B); higher B values indicate more compression resistance. Shear modulus (G) represents the ability to tolerate shape changes and shear deformation, as well as its stiffness against forces that cause angular distortion. Young's modulus (E) measures the stiffness under uniaxial stress. Table 5 shows the evaluated mechanical properties of Na_2InAgF_6, K_2InAgF_6, and Rb_2InAgF_6, and is illustrated in Fig. 3(b). These properties include their strength, elasticity, ductility, and thermal stability. These values were determined using the relationships described below:[61,62]

$$B = \frac{1}{2}(B_r + B_v) \quad (11)$$

$$G = \frac{1}{2}(G_r + G_v) \quad (12)$$

$$Y = \frac{9BG}{3B + G} \quad (13)$$

The bulk modulus demonstrates the maximum value in Na_2InAgF_6 (38.60 GPa), which decreases to 35.75 GPa for K_2InAgF_6 and subsequently to the lowest value observed in Rb_2InAgF_6 (32.75 GPa). The highest value of bulk modulus for Na_2InAgF_6 indicates that it is the most incompressible and mechanically stable material, which reflects stronger atomic bonding compared to the other two compounds. The shear modulus shows its highest value in Rb_2InAgF_6 (11.73 GPa), which is greater than K_2InAgF_6 (10.48 GPa) and Na_2InAgF_6 (9.88 GPa). This characteristic suggests that Rb_2InAgF_6 is the most resistant to shear forces and shape distortion, whereas Na_2InAgF_6 is the least resistant compound. Young's modulus, which measures stiffness, is also highest in Rb_2InAgF_6 (31.44 GPa), which shows a decrease in K_2InAgF_6 (28.65 GPa) and Na_2InAgF_6 (27.31 GPa). A higher value of Young's modulus

Table 5 Computed mechanical parameters including bulk modulus (B), shear modulus (G), Young's modulus (E), Poisson's ratio (ν), Pugh's ratio (B/G), anisotropy factor (A), and melting temperature (T_m)

Compounds	B (GPa)	G (GPa)	E (GPa)	ν	B/G	A	T_m (K)
Na_2InAgF_6	38.60	9.88	27.31	0.38	3.91	0.33	930
K_2InAgF_6	35.75	10.48	28.65	0.37	3.41	0.38	910
Rb_2InAgF_6	32.75	11.73	31.44	0.34	2.79	0.80	853
$K_2InAgCl_6$ (ref. 48)	30.02	8.55	23.43	0.37	3.51	0.68	—
$K_2InAgBr_6$ (ref. 48)	25.72	12.03	31.23	0.29	2.14	0.60	—
K_2InAgI_6 (ref. 48)	20.12	11.14	28.21	0.27	1.81	0.48	—

indicates greater stiffness and resistance to elastic deformation. Therefore, K_2InAgF_6 shows moderate flexibility with balanced stiffness and ductility.[63] The Poisson ratio, ν is the dimensional alteration of a material in directions perpendicular to stress application.[64] The B/G ratio demonstrates the ductility or brittleness of a material, with greater values of over 1.75 indicating ductility.[65] Mechanical anisotropy is present to a larger degree in materials exhibiting A factors that are not 1 in all directions.[66] The material's melting point in Kelvin indicates its thermal stability as given by T_m.[67] The following formulas are used to calculate these four parameters:

$$\vartheta = \frac{3B - 2G}{2(3B + G)} \quad (14)$$

$$A = \frac{2C_{44}}{C_{11} - C_{12}} \quad (15)$$

$$T_m = (554 + 5.911C_{11}) \pm 300\ \text{K} \quad (16)$$

Material's deformation under stress is quantified by Poisson's ratio (ϑ). Among all three studied compounds, Na_2InAgF_6 has the highest Poisson ratio of 0.38, followed by K_2InAgF_6 at 0.37 and Rb_2InAgF_6 at 0.34. Na_2InAgF_6 has a high ν value, indicating a large lateral expansion, which signifies better ductility compared to the rest of the compounds. The ductile *versus* brittle behaviour of materials is primarily determined by Pugh's ratio (B/G). Na_2InAgF_6 demonstrates the greatest ductility with a B/G value of 3.91, closely followed by K_2InAgF_6 at 3.41, whereas Rb_2InAgF_6 is the least ductile with 2.79. All compounds exhibit ductile behavior, as their B/G ratios exceed the critical value of 1.75 with different values as illustrated in Fig. 3(c).

Mechanical anisotropy is measured by the anisotropy factor (A), where 1 is ideal isotropy. Rb_2InAgF_6 (0.80) is the least anisotropic, making it the most mechanically uniform of the three compounds. Ahmad *et al.* reported similar elastic and mechanical properties for $K_2InAgCl_6$, $K_2InAgBr_6$, and K_2InAgI_6, which are in close agreement with our calculated values, thereby confirming the reliability of the present results.[48] The thermal stability is measured using the melting temperature (T_m). The highest T_m is exhibited by Na_2InAgF_6 at 930 K, followed by K_2InAgF_6 at 910 K, and Rb_2InAgF_6 at 853 K. The excellent thermal resistance of Na_2InAgF_6 makes it the most appropriate compound for applications at high temperatures, whereas Rb_2InAgF_6 is the least thermally stable. Overall, Na_2InAgF_6 demonstrated the best combination of ductility and thermal stability, while Rb_2InAgF_6 represented the lowest elastic anisotropy, indicating more isotropic mechanical behaviour. The elastic local anisotropy tool, ELATE[45] was used to create the three-dimensional visualizations of anisotropic Young's modulus (E), shear modulus (G), and Poisson ratio (ν) visualization of A_2InAgX_6 (A = Na, K, and Rb) shown in the Fig. 4.

3.3 Electronic properties

The band structure is a crucial element in the evaluation of materials' electronic properties. Band structures, including conductor, semiconductor, and insulator forms, can clarify the electrical properties of a material. The bandgap is the energy variation between the valence band maximum (VBM) and conduction band minimum (CBM) in a material's electronic band structure.[68] This study analyses the band structures depicted in Fig. 5, calculated using Generalized Gradient Approximation (GGA-PBE) both with and without SOC, as well as with the HSE06 functionals for three halide double perovskites, A_2InAgF_6 (A = Na, K, and Rb). The Band Structure diagrams of A_2InAgF_6 (A = Na, K, and Rb) demonstrate that the VBM and CBM align exactly at the highest symmetry k-point, known as the G point, within the first Brillouin zone. Within GGA-PBE, the calculated direct bandgaps are 0.98 eV, 1.52 eV, and 1.70 eV for Na_2InAgF_6, K_2InAgF_6, and Rb_2InAgF_6, respectively. The impact of relativistic spin orbit coupling (SOC) on the electronic structure is depicted in the top panels of Fig. 5. The inclusion of SOC breaks the degeneracy of several electronic states, with a noticeable effect in the valence band near the M point for A_2InAgF_6 (A = Na, K, and Rb). Furthermore, SOC causes a significant shift in the conduction band, lowering its energy, which leads to a considerable narrowing of the bandgap. As a result, the bandgaps calculated with SOC are consistently smaller than those predicted without SOC. This reduction becomes more pronounced with the substitution of heavier A-site atoms, reflecting the stronger relativistic effects associated with higher atomic numbers. Specifically, the bandgap of Na_2InAgF_6 decreases from 0.98 eV to 0.59 eV with SOC inclusion, while for K_2InAgF_6, it is significantly reduced from 1.52 eV to 1.18 eV, and for Rb_2InAgF_6, it decreases from 1.70 eV to 1.42 eV. The substantial reduction in the bandgap observed in A_2InAgF_6 (A = Na, K, and Rb) compounds underscores the importance of including SOC for accurately describing the electronic properties of halide perovskites containing heavier elements like In and Ag, as SOC can notably modify the band dispersion and reduce the bandgap.

As expected, the HSE06 functional yields larger and more accurate bandgaps of 3.02 eV, 3.63 eV, and 3.88 eV for Na_2InAgF_6, K_2InAgF_6, and Rb_2InAgF_6, respectively as shown in Table 6. The atomic radius increases in the order: Na < K < Rb. Due to differences in atomic shapes and sizes, the bandgap varies, rising from sodium to potassium and rubidium to regulate the total repulsion among the electronic states.[69] Direct bandgap double halide perovskites provide substantial benefits for optoelectronic applications owing to their effective light absorption and emission characteristics. These attributes render them exceptionally appealing for next-generation solar cells, LEDs, and various photonic gadgets.[70]

The Density of States (DOS) diagrams offer critical insights into the electronic structures of the A_2InAgF_6 (A = Na, K, and Rb) compounds by depicting both Total Density of States (TDOS) and Partial Density of States (PDOS) across a wide energy spectrum. Fig. 6 illustrates the DOS profiles for the three variants, spanning energies from −10 eV to +10 eV, with the Fermi level (E_f) positioned at 0 eV, separating the occupied and unoccupied states. A detailed observation reveals characteristic features in both the valence and conduction bands, helping determine the bonding nature and electronic conductivity of each composition. In the lower valence region, strong peaks

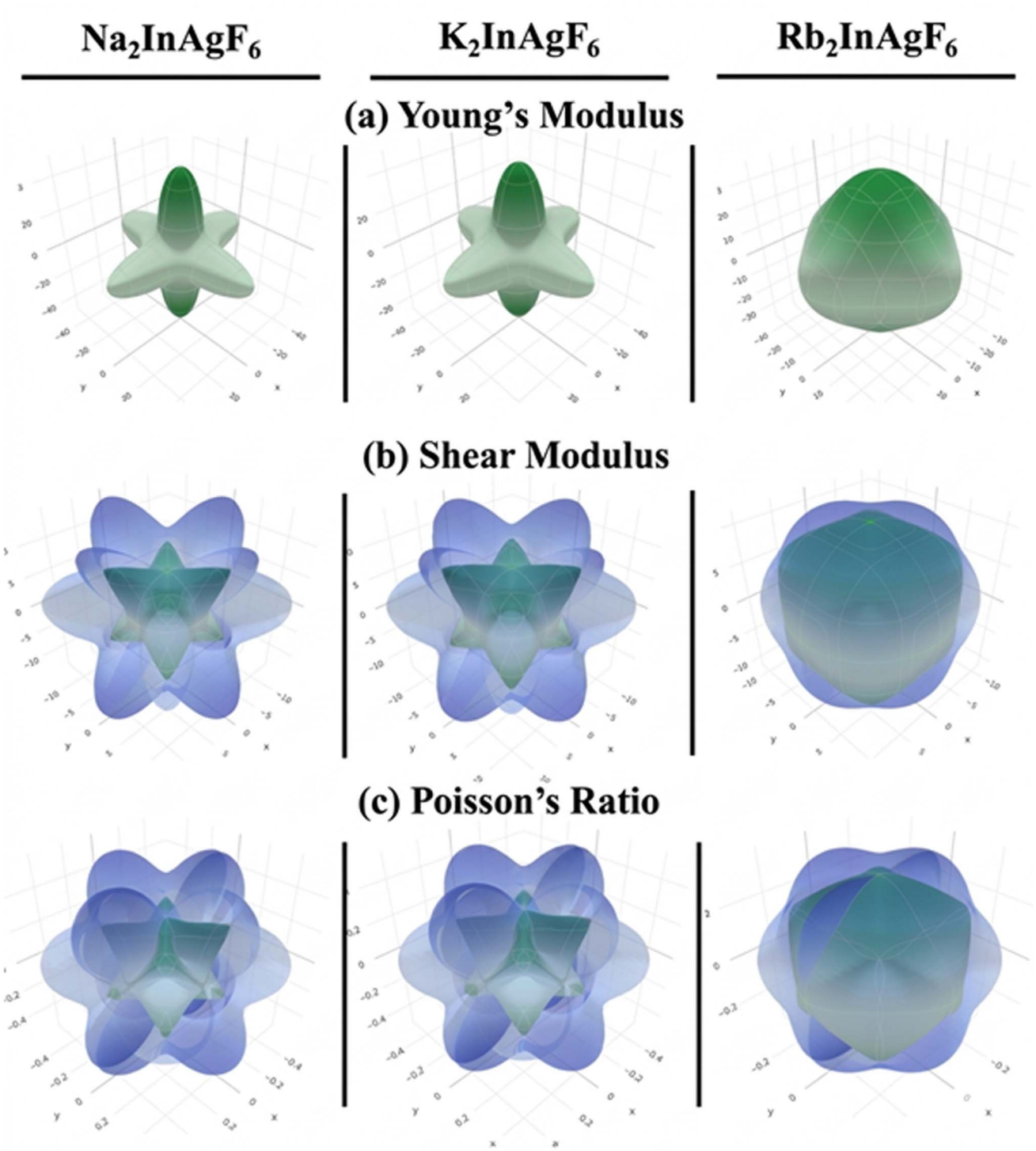

Fig. 4 The physical properties of the elastic parameters of A_2InAgF_6 (A = Na, K, and Rb) (a) Young's modulus, (b) shear modulus, and (c) Poisson's ratio are described in the 3D illustration.

appear. These peaks come from the hybridization between F-2p and Ag-4d orbitals. This shows the presence of strong covalent bonding. The p-states of the A-site cations (Na, K, Rb) appear only weakly. They stay localized in shallow energy ranges. This means they have only a small role in electronic interactions. The conduction band begins just above 0 eV and goes up to +10 eV. The conduction band mainly consists of contributions from In-5s, Ag-5s, and F-2p orbitals. There are clear differences in the start of conduction for the three compounds. From the DOS curves, the bandgaps are estimated. Rb_2InAgF_6 has the widest bandgap of 3.88 eV. This means it has very few electronic states near the Fermi level and is less conductive. K_2InAgF_6 shows

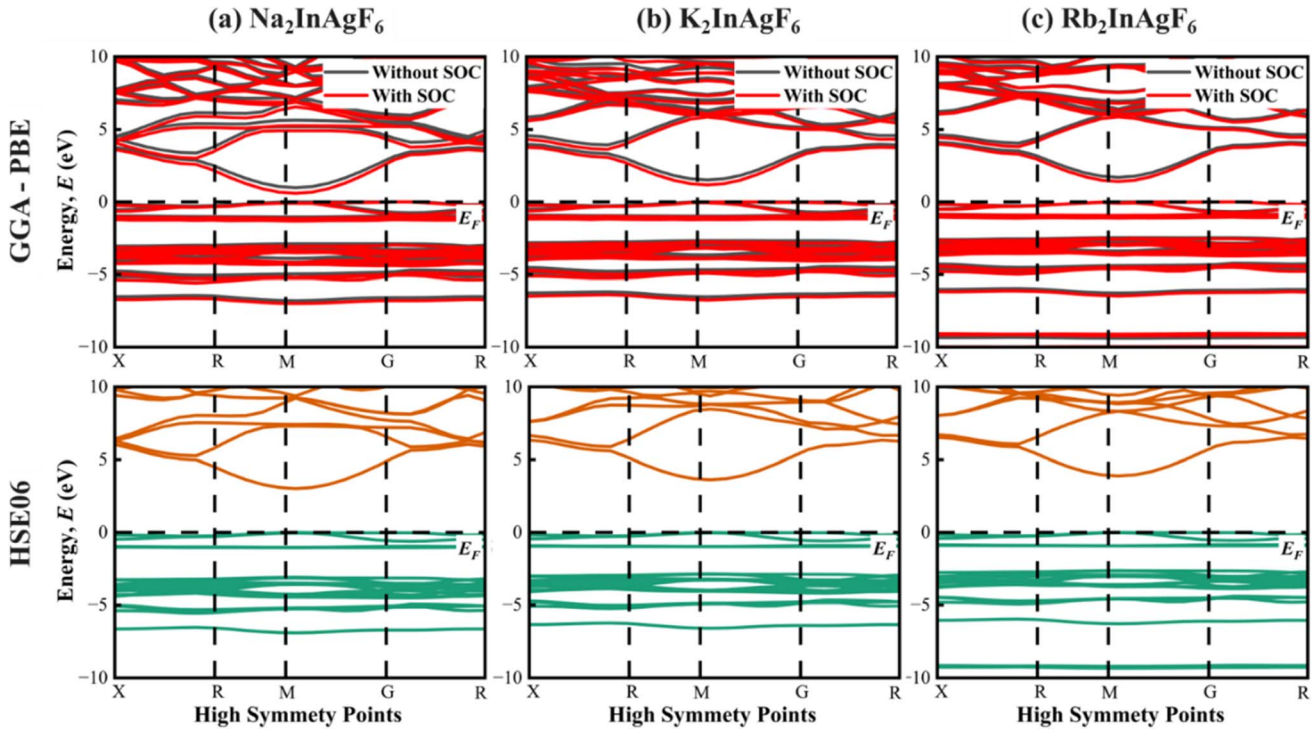

Fig. 5 Calculated band structure of (a) Na_2InAgF_6, (b) K_2InAgF_6, (c) Rb_2InAgF_6 using GGA-PBE with and without spin–orbit coupling (SOC) and calculated band structure using Hybrid-HSE06 functional.

a moderate bandgap of 3.63 eV. Na_2InAgF_6 has the smallest bandgap of 3.02 eV. This shows it has the highest density of conduction states near E_F. The bandgap becomes smaller as the A-site cation decreases in size from Rb^+ to Na^+. The reduction happens because smaller cations cause more structural distortion and stronger orbital overlap between Ag-F and In-F. This makes electronic excitation easier. Based on these bandgaps, the expected order of conductivity is: Rb_2InAgF_6 < K_2InAgF_6 < Na_2InAgF_6. Na_2InAgF_6 is therefore expected to exhibit the highest intrinsic conductivity. However, the relatively sharp density of states features near the conduction band edge in Na_2InAgF_6 indicate favorable charge transport characteristics, making it a promising candidate for optoelectronic device applications requiring balanced transport properties. On the other hand, Rb_2InAgF_6 has a wide bandgap and low conduction. It may be more useful in applications that need high resistivity or insulating properties. The PDOS confirms the active roles of Ag-d, In-p, and F-p orbitals in shaping the electronic structure of these compounds.

The effective mass (m^*) of charge carriers in the A_2InAgF_6 (A = Na, K, Rb) series was evaluated to determine the electronic transport properties, as it is inversely proportional to the curvature of the energy bands according to the relation:

$$m^* = \hbar^2 \left(\frac{d^2 E(k)}{dk^2} \right)^{-1} \quad (17)$$

where $E(k)$ and $\hbar$ are band energy as a function of the wave vector k and reduced Planck constant, respectively. The HSE06 calculations reveal a consistent electron effective mass (m_e^*) of 0.10 across all three compounds, indicating a highly dispersive conduction band minimum (CBM) that favors high n-type mobility. Conversely, the hole effective masses (m_h^*) are

Table 6 The computed bandgap and effective mass of the carriers of A_2InAgF_6 (A = Na, K, and Rb) compounds

	Bandgap (eV)				Effective mass	
	GGA-PBE				HSE06	
Compounds	Without SOC	With SOC	Previous study (mbj-PBE sol)	HSE06	m_e^*	m_h^*
Na_2InAgF_6	0.98	0.59	—	3.02	0.10	0.82
K_2InAgF_6	1.52	1.18	—	3.63	0.10	0.86
Rb_2InAgF_6	1.70	1.42	—	3.88	0.10	0.94
$K_2InAgCl_6$ (ref. 48)	—	—	2.48	—	—	—
$K_2InAgBr_6$ (ref. 48)	—	—	1.47	—	—	—
K_2InAgI_6 (ref. 48)	—	—	0.23	—	—	—

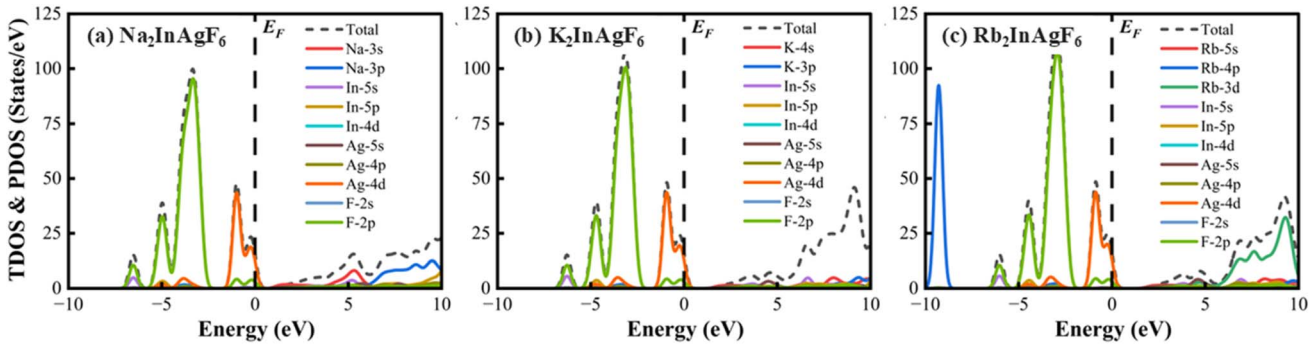

Fig. 6 The Total Density of States (TDOS) and Partial Density of States (PDOS) of the compounds (a) Na_2InAgF_6, (b) K_2InAgF_6, and (c) Rb_2InAgF_6.

significantly higher, ranging from 0.82 for Na_2InAgF_6 to 0.94 for Rb_2InAgF_6, suggesting a flatter valence band maximum (VBM) and potentially restricted p-type transport. This pronounced asymmetry between m_e^* and m_h^* implies that while these halides are excellent candidates for electron conduction, the relatively heavy holes may limit overall bipolar charge extraction efficiency in optoelectronic applications. Furthermore, the marginal increase in m_h^* from Na to Rb correlates with the widening of the bandgap from 3.02 eV to 3.88 eV, reflecting the influence of the A-site cation on the electronic structure.

The Electron Localization Function (ELF) analysis quantifies the charge distribution within a given region of space. The ELF analysis shown in Fig. 7 along the (100) and (200) crystallographic planes provide valuable insights into the physical properties and bonding characteristics of A_2InAgF_6 (A = Na, K, and Rb) double perovskites. The charge density map on the right side of Fig. 7 uses a color scale where red areas represent higher electron density, reaching up to 0.4713 e $Å^{-3}$, and blue areas indicate lower electron density approaching 0 e $Å^{-3}$. The presence of overlapping elliptical contours between In and F atoms on the (100) plane confirms covalent bonding. In contrast, spherical contours around Ag and F atoms on the (200) plane, with no atomic overlap, suggest that ionic bonding predominates.

3.4 Optical properties

The optical characteristics prescribe how the materials interact with electromagnetic (EM) radiation, which includes absorption, reflection, transmission, and optical conductivity. An overall knowledge of these properties has been vital in the design and optimization of materials in the optoelectronic structures, such as solar cells, light emitting diodes (LEDs), and photodetectors.[71] The optical parameters of A_2InAgF_6 (A = Na, K, and Rb) have been determined at photon energies of 30 eV, revealing the regulation of the material's optical characteristics.

A convergence test with respect to the *k*-point mesh was performed to ensure the accuracy and reliability of the optical

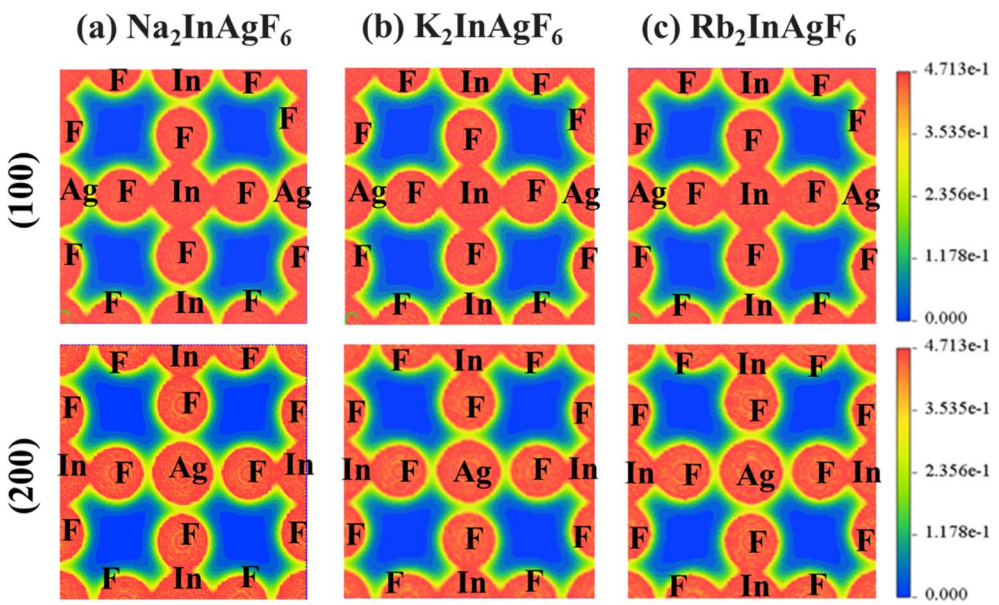

Fig. 7 Electron localization function (ELF) analysis along the (100) and (200) crystallographic plane of (a) Na_2InAgF_6, (b) K_2InAgF_6, and (c) Rb_2InAgF_6.

spectra. The optical properties of Na_2InAgF_6 were calculated using *k*-point meshes of 4 × 4 × 4, 6 × 6 × 6, 8 × 8 × 8, and 10 × 10 × 10. The results showed that the optical spectra for the 8 × 8 × 8 and 10 × 10 × 10 *k*-point meshes were nearly identical, as shown in Fig. 8, indicating that increasing the *k*-point mesh beyond 8 × 8 × 8 does not significantly affect the calculated optical properties. That's why this *k*-point mesh was subsequently used for the calculation of the optical properties for all other A_2InAgF_6 (A = Na, K, and Rb) compounds.

3.4. 1 Dielectric functions. The dielectric function is an indispensable quantity for analyzing the optical properties, which are related to absorption characteristics, as indicated by the following equation for materials:

$$\varepsilon(\omega) = \varepsilon_1(\omega) + i\varepsilon_2(\omega) \quad (18)$$

Here, $\varepsilon_1(\omega)$ represents the dielectric constant (real part), while $\varepsilon_2(\omega)$ denotes the imaginary part. The dielectric function physically represents the frequency-dependent relative permittivity of the material. The material's ability to polarize and reflect incident light is governed by $\varepsilon_1(\omega)$, while optical absorption is primarily described by $\varepsilon_1(\omega)$, which also influences device performance. The capacity of a material to dissipate energy is dictated by its $\varepsilon_2(\omega)$, which also confirms its appropriateness for a certain application within a defined energy spectrum.[72] The real dielectric function $\varepsilon_1(\omega)$ and imaginary dielectric function $\varepsilon_2(\omega)$ defined as:

$$\varepsilon_1(\omega) = 1 + \frac{2}{\pi} P \int_0^{\infty} \frac{\omega' \varepsilon_2(\omega)}{\omega'^2 - \omega^2} d\omega' \quad (19)$$

$$\varepsilon_2(\omega) = \frac{e^2}{\pi m^2 \omega^2} \sum \int |M_{V,C}(k)|^2 \delta[\omega_{VC}(k) - \omega] d^3k \quad (20)$$

Here, P denotes the momentum matrix element between the electronic states of bands α and β under the crystal momentum k.

The comparatively larger $\varepsilon_1(0)$ values are associated with the materials' narrower bandgaps, which are useful for minimizing carrier recombination rates and improving optoelectronic device efficacy.[73] Fig. 9(a) indicates the dielectric function of A_2InAgF_6 (A = Na, K, and Rb) compounds. The real component of the static dielectric function $\varepsilon_1(0)$, for the evaluated double perovskites, is summarized as follows: $\varepsilon_1(0)$ = 1.55 for Na_2InAgF_6, $\varepsilon_1(0)$ = 1.64 for K_2InAgF_6, and $\varepsilon_1(0)$ = 1.74 for Rb_2InAgF_6. As the photon energy increases, the real part $\varepsilon_1(\omega)$ initially rises to a maximum in the low-energy region (~5–8 eV) and then gradually decreases, eventually attaining negative values at higher energies. This behavior indicates a transition from dielectric to metallic-like response due to strong electronic excitations. Among the studied compounds, Rb_2InAgF_6 exhibits the most intense peak, indicating enhanced optical polarization, while K_2InAgF_6 and Na_2InAgF_6 show comparatively lower and broader peaks, reflecting reduced polarization strength.

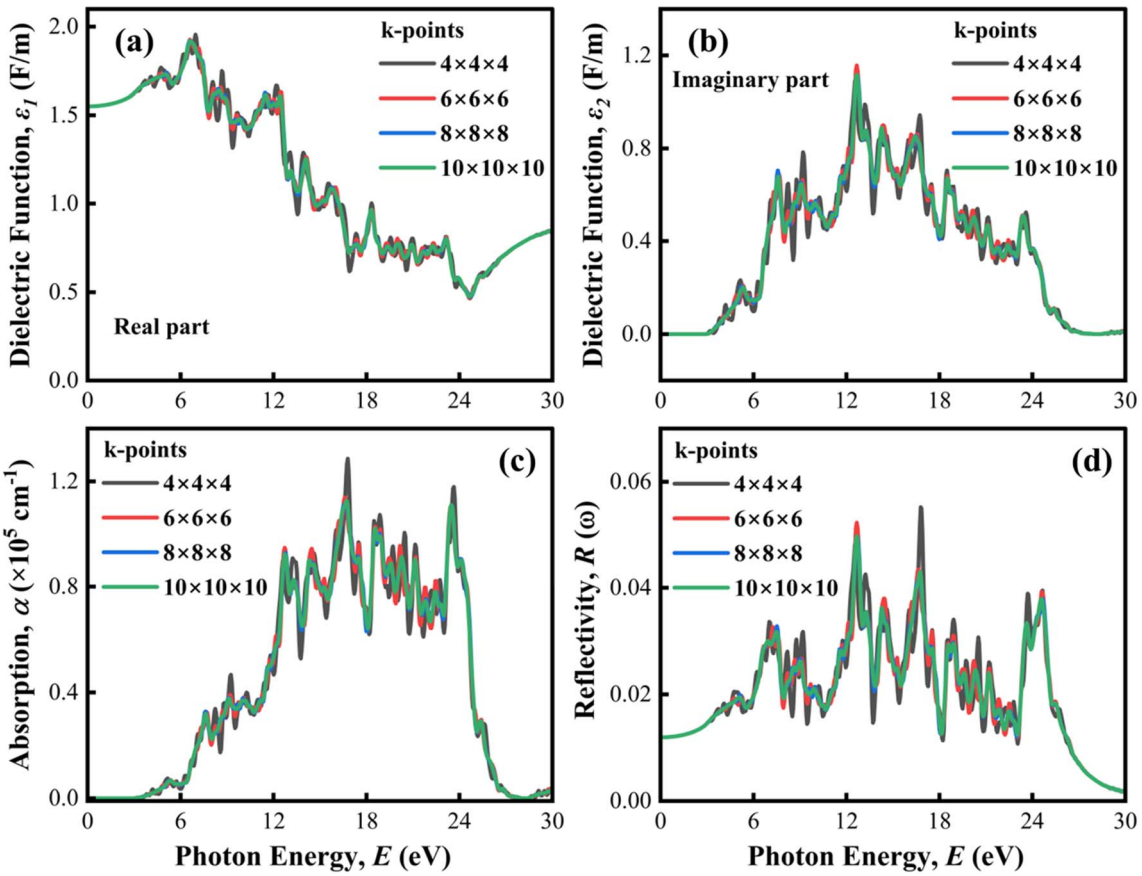

Fig. 8 The convergence test of *k*-point mesh for the calculation of (a) real part, (b) imaginary part of the dielectric function, (c) absorption, and (d) reflectivity of Na_2InAgF_6 calculated using *k*-point meshes of 4 × 4 × 4, 6 × 6 × 6, 8 × 8 × 8, and 10 × 10 × 10.

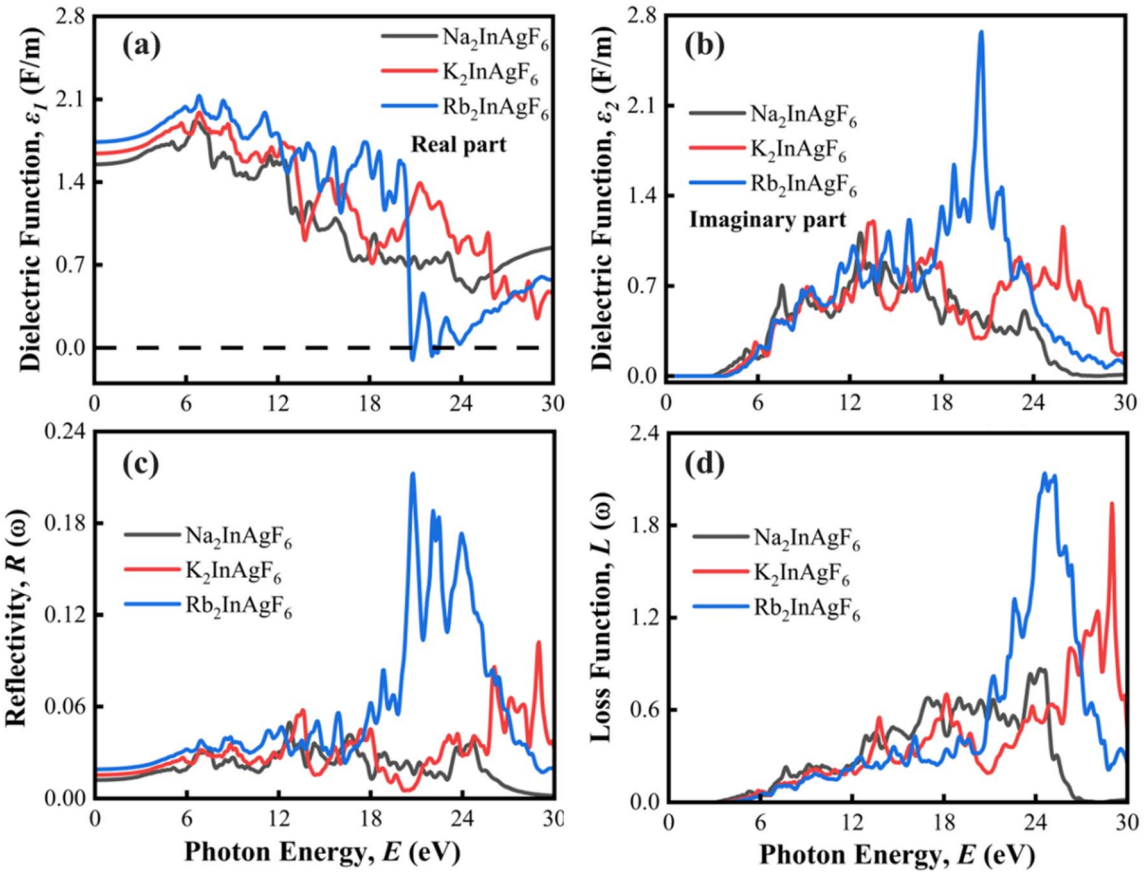

Fig. 9 The visualization of the A_2InAgF_6 (A = Na, K, and Rb) compounds' (a) real part, (b) imaginary part of the dielectric function, (c) reflectivity, and (d) loss function.

The imaginary part of the dielectric function, $\varepsilon_2(\omega)$, provides important information about interband electronic transitions between the valence and conduction bands. From Fig. 9(b), $\varepsilon_2(\omega)$, remains nearly zero up to the bandgap energy for all compounds, indicating the absence of optical transitions in this region. As the photon energy exceeds the bandgap, $\varepsilon_2(\omega)$, increases sharply and exhibits multiple pronounced peaks, corresponding to strong optical transitions. Rb_2InAgF_6 shows the highest peak intensity (~2.67 near ~20.6 eV), followed by K_2InAgF_6 and Na_2InAgF_6. These variations arise from differences in their electronic band structures and transition probabilities. Overall, the dielectric response confirms strong optical activity in the UV region, highlighting their potential for optoelectronic applications.

3.4. 2 Reflectivity. Reflectivity in density functional theory (DFT) refers to the portion of incident light reflected by a substance's surface, based upon the material's electronic structure. This property can be determined using the following equation:

$$R(\omega) = \frac{(n-1)^2 + k^2}{(n+1)^2 + k^2} \quad (21)$$

Fig. 9(c) presents an analysis of the reflectance spectra for A_2InAgF_6 (A = Na, K, and Rb) double halide perovskite compounds. The obtained static coefficients of reflection R (0) are 0.011, 0.015, and 0.018 for A_2InAgF_6 (A = Na, K, and Rb) compounds, respectively. With increasing photon energy, $R(\omega)$ shows peaks due to interband transitions. Rb_2InAgF_6 has the highest reflectivity (~0.212 at ~20.6 eV), K_2InAgF_6 shows moderate peaks (~0.101 at ~28.9 eV), while Na_2InAgF_6 remains lower (0.049). Low visible-region reflectivity and moderate UV values suggest efficient absorption, making these materials suitable for optoelectronic applications.

3.4. 3 Loss function. The loss function represents fundamental insights into plasmonic events and dielectric responses by specifying the mechanisms *via* which electrons dissipate energy during interactions with external electromagnetic fields.[74] The computation is done according to the equation as shown below:

$$L(\omega) = \frac{\varepsilon_2(\omega)}{\varepsilon_1^2(\omega) + \varepsilon_2^2(\omega)} \quad (22)$$

Fig. 9(d) shows the energy loss function $L(\omega)$, representing electron energy dissipation. All compounds exhibit low loss at low photon energies and prominent peaks at higher energies. The main peaks appear around ~24.7 eV for Rb_2InAgF_6, ~24.5 eV for Na_2InAgF_6, and ~29 eV for K_2InAgF_6, indicating plasma resonance. Rb_2InAgF_6 shows the highest intensity

(~2.07), followed by K_2InAgF_6 (~1.86), while Na_2InAgF_6 has lower values (~0.85). These peaks correlate with optical conductivity and reflect collective electronic excitations. The low loss in the visible region and strong high-energy peaks suggest reduced energy dissipation, highlighting their potential for optoelectronic and photovoltaic applications.

3.4. 4 Refractive index. The index refraction of a substance is a significant characteristic for assessing photon absorption during the chemical degradation process in mixtures. A high refractive index is correlated with a denser medium, as documented in an earlier study.[75] Complex refractive index ($n + ik$) is an important characteristic of a solid material, giving information about the velocity with which light travels, and has prospective uses in optoelectronics.[76] The calculations follow the equation stated below:

$$n(\omega) = \left[\frac{\left\{\sqrt{\varepsilon_1{}^2(\omega) + \varepsilon_2{}^2(\omega)}\right\} - \varepsilon_1(\omega)}{2}\right]^{\frac{1}{2}} \quad (23)$$

Applying eqn (17), the actual components of the complex refractive index were obtained. The value of $n(\omega)$ fluctuates based on the material, although semiconductors often have a low $k(\omega)$. The refractive index $n(\omega)$ of A_2InAgF_6 (A = Na, K, Rb) shown in Fig. 10(a) follows a trend similar to the real part of the dielectric function, $\varepsilon_1(\omega)$. At zero photon energy, the static refractive indices are about 1.25, 1.28, and 1.32 for Na_2InAgF_6, K_2InAgF_6, and Rb_2InAgF_6, respectively. With increasing photon energy, $n(\omega)$ shows small peaks in the low-energy region (~6–10 eV), reaching ~1.4–1.45, and then gradually decreases, becoming less than unity at higher energies due to reduced polarization and strong dispersion. This behavior indicates normal dispersion at low energies and anomalous dispersion at higher energies. The moderate refractive index values suggest good transparency and confirm the dielectric nature of these compounds, making them suitable for optoelectronic applications.

3.4. 5 Extinction coefficient. The extinction coefficient, $k(\omega)$, can be defined to measure the loss of electromagnetic radiation through material expression. As can be seen in Fig. 10(b), the calculated $k(\omega)$ of A_2InAgF_6 (A = Na, K, and Rb) has a trend that is similar to that of the imaginary component of the dielectric function, $\varepsilon_2(\omega)$. This correspondence spells the direct correlation between optical absorption with $k(\omega)$, seeing that $\varepsilon_2(\omega)$ is the capacity of the material to be able to absorb photon energy.

A_2InAgF_6 exhibits the highest peak (~1.1 at ~20–21 eV), followed by K_2InAgF_6 (~0.6 at ~25–26 eV), and Na_2InAgF_6 shows lower values (~0.4). Multiple peaks in the 18–26 eV range indicate various interband transitions in Fig. 10(b). Overall, strong UV response and low visible absorption highlight their suitability for ultraviolet optoelectronic applications.

3.4. 6 Conductivity. Optical conductivity $\sigma(\omega)$ is a crucial parameter that indicates the response of charge carriers at optical frequencies. The optical conductivity of a material is intrinsically linked to its electronic band structure, as it originates from interband electronic transitions. Optical conductivity arising from interband electronic transitions within the visible to ultraviolet energy range is essential for optoelectronic applications.[77] Substitution of alkali metals exerts only a minor influence on the optical conductivity within the visible spectrum. The conductivity was obtained using the following equation:

$$\sigma(\omega) = \frac{\alpha(\omega)n(\omega)c}{4\pi} \quad (24)$$

Fig. 11(a) and (b) show the real and imaginary parts of the optical conductivity, $\sigma_1(\omega)$ and $\sigma_2(\omega)$, of A_2InAgF_6 (A = Na, K, and Rb). The real part $\sigma_1(\omega)$ indicates charge transport due to photon absorption. All compounds exhibit negligible conductivity at low energies (visible region), confirming insulating behavior, while conductivity increases sharply in the UV region due to enhanced interband transitions. Rb_2InAgF_6 shows the highest peak (~6.66 (fs^{-1}) at ~20.6 eV), followed by K_2InAgF_6 (~3.63 (fs^{-1}) at ~25.5 eV), whereas Na_2InAgF_6 exhibits lower (~1.7 (fs^{-1}) at ~12.7 eV) and broader peaks. The imaginary part σ_2 (ω) reflects energy storage and dissipation. It remains negative at low energies,

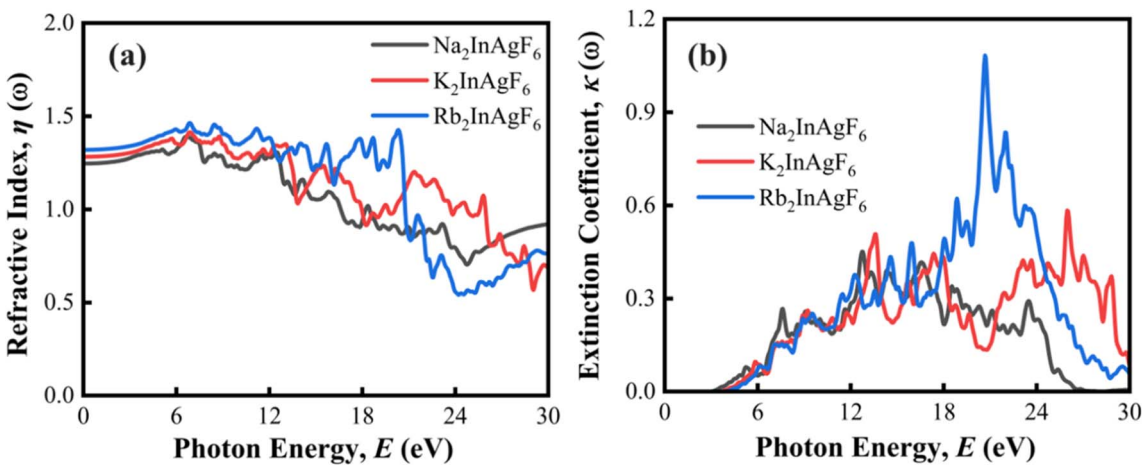

Fig. 10 The visualization of the A_2InAgF_6 (A = Na, K, and Rb) compounds' (a) refractive index, and (b) extinction coefficient.

indicating weak optical response, and becomes positive at higher energies with multiple oscillations, especially in the 18–28 eV range. Rb_2InAgF_6 again shows the highest intensity (~2.5–2.7 (fs^{-1})), followed by K_2InAgF_6 and Na_2InAgF_6. Overall, the absence of conductivity in the visible region and strong response in the UV region confirm their wide bandgap nature and suitability for ultraviolet optoelectronic applications.

3.4. 7 Absorption coefficient. The effectiveness of optoelectronic and photovoltaic devices is significantly determined by their capacity to absorb sunlight, as the creation and transportation of charge carriers are directly correlated with the absorption coefficient.[78] The absorption coefficient $\alpha(\omega)$ is essential for describing the mechanisms by which materials absorb photons and generate pairs of electrons and holes, which is vital for the operation of photovoltaic devices such as solar cells. An increased absorption coefficient results in enhanced light absorption and a more significant decrease in the intensity of light passing. This eventually boosts the device's efficiency. This is calculated by the equation:

$$\alpha(\omega) = \frac{4\pi K}{\lambda} \quad (25)$$

The absorption coefficient $\alpha(\omega)$ of A_2InAgF_6 (A = Na, K, Rb) in Fig. 11(c) shows clear dependence on the A-site cation, with slight shifts in the absorption edge indicating variation in optical bandgaps. Na_2InAgF_6 exhibits the earliest onset, followed by K_2InAgF_6 and Rb_2InAgF_6. All compounds display weak absorption at low energies and strong absorption in the ultraviolet (UV) region. Rb_2InAgF_6 shows the highest peak (~3.61 × 10^5 cm^{-1} at ~21–22 eV), followed by K_2InAgF_6 (~2.45 × 10^5 cm^{-1} at ~26 eV), while Na_2InAgF_6 has the lowest intensity (~1.1 × 10^5 cm^{-1}). Multiple peaks in the 18–26 eV range indicate various interband electronic transitions, arising from differences in their band structures. Negligible absorption in the visible region suggests transparency to visible light. The overall behavior of $\alpha(\omega)$ follows $\varepsilon_2(\omega)$, with minor deviations due to the independent-particle approximation. The strong UV absorption highlights their potential for ultraviolet optoelectronic applications.

A comparable analysis of dielectric response, absorption, and optical behavior has been reported by Shah *et al.*[79] for halide double perovskites, highlighting the strong dependence of optical properties on compositional variation. The A_2InAgF_6 (A = Na, K, and Rb) compounds exhibit a systematic enhancement in optical properties with increasing A-site cation size, where Rb_2InAgF_6 demonstrates the strongest dielectric response, absorption, and optical conductivity, indicating superior ultraviolet optoelectronic performance. Substituting

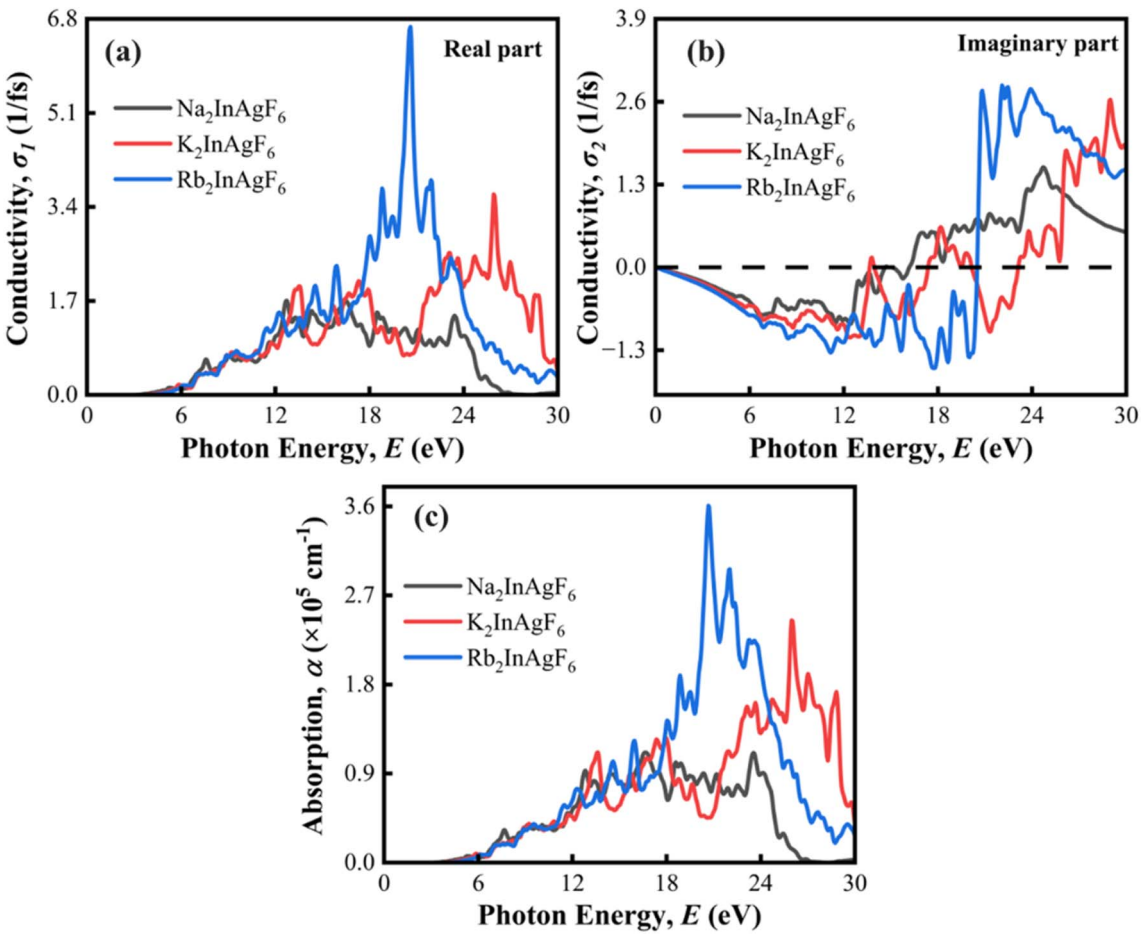

Fig. 11 The visualization of the A_2InAgF_6 (A = Na, K, and Rb) compounds' (a) real part, (b) imaginary part of conductivity, and (c) absorption.

the halide with hydrogen may enable these compounds to function as hydrogen storage materials.[80] Beside double perovskite[80] A_2B_7- and AB_2-type materials also used for hydrogen storage (Table 7).[81,82]

3.5 Phonon dispersion and thermodynamic properties

The dynamic stability of these double perovskites is analyzed by their phonon dispersion spectra. The calculated phonon spectra of A_2InAgF_6 (A = Na, K, and Rb) along the high-symmetry paths (X–R–M–G–R) in the Brillouin zone are shown in Fig. S1. The presence of imaginary frequencies in a material's phonon dispersion is a key indicator of dynamic instability at 0 K. Conversely, a lattice is considered dynamically stable if all its phonon frequencies are real and positive. As there are imaginary frequencies of Na_2InAgF_6, K_2InAgF_6 and Rb_2InAgF_6 phonon spectra, it shows the dynamic instability of them leading to significant structural changes at certain temperatures. Importantly, theoretical dynamical instabilities at 0 K do not necessarily rule out experimental feasibility. For example, the well-known perovskite $BaTiO_3$ exhibits imaginary phonon modes in its cubic phase at 0 K, yet it becomes dynamically stable at finite temperatures due to anharmonic lattice vibrations and thermal effects.[83] Similarly, compounds such as AlH_3,[84] superconducting Y_2C_3,[85] and high-pressure H_3S[86] have been predicted to display dynamical instabilities in theoretical studies, but have nonetheless been successfully synthesized and experimentally characterized. In the present work, all A_2InAgF_6 (A = Na, K, and Rb) compounds exhibit negative formation enthalpies and satisfy the Born mechanical stability criteria, indicating their intrinsic thermodynamic and mechanical stability. Therefore, the observed imaginary phonon modes may suggest a tendency toward lower-symmetry structures, which could be stabilized under finite-temperature conditions.

Thermodynamic properties are the measurable parameters of a system that describe its state and the surrounding environment. The thermodynamic properties of Na_2InAgF_6, K_2InAgF_6, and Rb_2InAgF_6 compounds are systematically analyzed to comprehend their vibrational and thermal behaviour. These properties, including enthalpy, entropy, free energy, heat capacity, and Debye temperature, are estimated using density functional perturbation theory across the temperature range of 0–1000 K.

The parameters are determined from the phonon density of states $g(\omega)$ according to the following relations:

$$H(T) = E_{\text{tot}} + \frac{1}{2}\int g(\omega)\hbar\omega \, \mathrm{d}\omega + \int \left(\hbar\omega \Big/ \left(\frac{\hbar\omega}{e^{\frac{\hbar\omega}{k_B T}} - 1} \right) \right) g(\omega) \, \mathrm{d}\omega \tag{26}$$

$$S(T) = k_B \left[\int \frac{\hbar\omega}{e^{\frac{\hbar\omega}{k_B T}} - 1} g(\omega) \mathrm{d}\omega - \int g(\omega) \ln\left(1 - e^{\frac{\hbar\omega}{k_B T}}\right) \mathrm{d}\omega \right] \tag{27}$$

$$F(T) = E_{\text{tot}} + \frac{1}{2}\int g(\omega)\hbar\omega \, \mathrm{d}\omega + k_B T \int g(\omega) \ln\left(1 - e^{\frac{\hbar\omega}{k_B T}}\right) \mathrm{d}\omega \tag{28}$$

where k_B is the Boltzmann constant. As shown in Fig. 12(a), the enthalpy increases monotonically with temperature for all studied compounds. This behaviour indicates the accumulation of vibrational energy with increasing thermal energy. Among the materials, Rb_2InAgF_6 shows the highest enthalpy at elevated temperatures, which may be attributed to its heavier cationic mass and greater unit-cell energy storage capability. As depicted in Fig. 12(a), the entropy increases with temperature, which is consistent with the increasing vibrational disorder and population of phonon modes at higher temperatures. Among the examined systems, Rb_2InAgF_6 shows a slightly higher entropy, reflecting enhanced vibrational degrees of freedom compared to Na_2InAgF_6 and K_2InAgF_6. The free energy, as illustrated in Fig. 12(b), exhibits a decreasing trend with temperature. This decrease results from the growing entropy contribution to the Helmholtz free energy, which dominates at higher temperatures and reduces the total free energy. The negative values throughout the temperature range confirm the thermodynamic stability of these compounds. Fig. 12(c) displays the heat capacity behaviour as a function of temperature. A rapid rise is observed initially, levelling off at higher temperatures, consistent with the Dulong–Petit law for classical solids. The slightly lower saturation heat capacity of Rb_2InAgF_6 may be associated with its distinctive lattice stiffness and phonon cut-off frequencies. In line with the third law of thermodynamics, all the calculated thermodynamic functions approach zero as the temperature approaches absolute zero, reflecting the disappearance of lattice vibrations in a perfectly ordered state. The Debye temperature has been measured to see if the compounds were good enough to be used

Table 7 Key optical properties of A_2InAgF_6 (A = Na, K, and Rb)

Optical property	Na_2InAgF_6	K_2InAgF_6	Rb_2InAgF_6
Static dielectric constant, $\varepsilon_1(0)$	1.55	1.64	1.74
Maximum imaginary dielectric function, $\varepsilon_2(\omega)$	~2.1	~2.4	~2.67
Static reflectivity, $R(0)$	0.011	0.015	0.018
Maximum reflectivity, $R(\omega)$	0.049	0.101	0.212
Static refractive index, $n(0)$	1.25	1.28	1.32
Maximum extinction coefficient, $k(\omega)$	0.4	0.6	1.1
Maximum absorption coefficient, α (cm^{-1})	1.1×10^5	2.45×10^5	3.61×10^5
Maximum optical conductivity, $\sigma_1(\omega)$	1.7	3.63	6.66

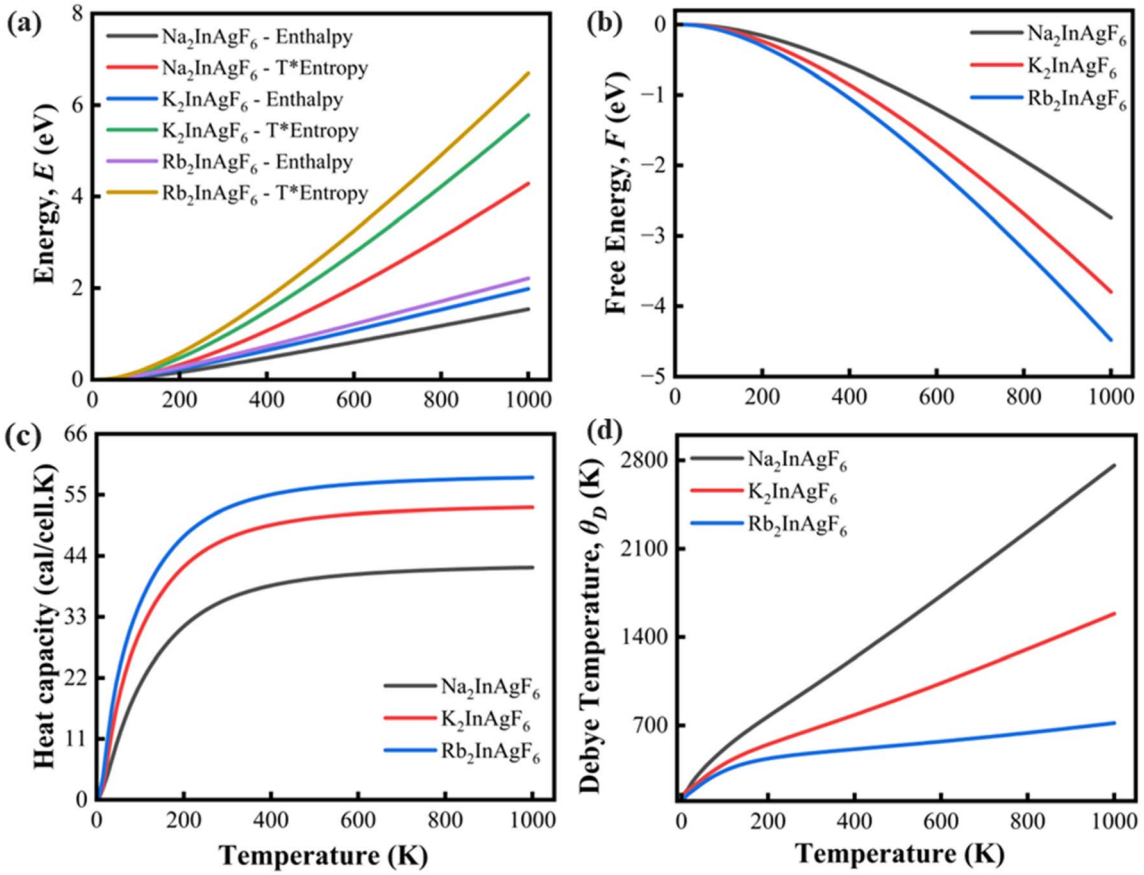

Fig. 12 The visualization of the A_2InAgF_6 (A = Na, K, and Rb) compounds' (a) enthalpy and entropy, (b) free energy, (c) heat capacity, and (d) Debye temperature.

in industrial equipment, as illustrated in Fig. 12(d). The Debye temperature (θ_D) is the highest temperature at which a crystal can vibrate in its normal way. It is a key factor in connecting a solid's elastic and thermodynamic properties, like its melting point, specific heat, and vibrational entropy. It was calculated by utilizing an equation that has already been published to find the average sound velocity by adding up the elastic wave velocities in the crystal.[87]

$$\theta_D = \frac{h}{k}\left[\frac{3n}{4\pi}\left(\frac{N_A\rho}{M}\right)\right]^{\frac{1}{3}} v_m \quad (29)$$

The symbols h and k, respectively, are used to denote Planck's and Boltzmann's constants. In addition, the symbols N_A, n, M, and ρ represent the numerical values of Avogadro's number, the number of atoms present in the unit cell, the molecular mass, and the density, respectively. When calculating the velocity of the sound (v_m), it is possible to utilize both the transverse (v_t) and longitudinal (v_l) sound velocities.

$$v_m = \left[\frac{1}{3}\left(\frac{2}{v_s^3} + \frac{1}{v_l^3}\right)\right]^{-1/3} \quad (30)$$

$$v_t = \sqrt{\frac{G}{\rho}} \quad (31)$$

$$v_l = \sqrt{\frac{3B + 4G}{3\rho}} \quad (32)$$

Debye temperature increases in a linear manner as temperature increases. At elevated temperatures, it is evident that Na_2InAgF_6 exhibits the highest Debye temperature among the three compounds.

4 Conclusion

This research provides a comprehensive theoretical investigation into the influence of A-site cation substitution on the physical properties of fluoride-based double perovskites A_2InAgF_6 (A = Na, K, and Rb). All three compounds are structurally stable, with the Rb-based variant exhibiting the highest stability based on its highly negative formation energy. The lattice parameters and unit cell volumes expand predictably with the increasing ionic size of the A-site cation. The compounds are identified as semiconductors with direct bandgaps ranging from 3.02 to 3.88. The bandgap is tunable through A-site cation engineering, where smaller cations (Na) result in smaller gaps due to structural distortion and stronger orbital overlap. The electron localization function analysis indicated a mixed covalent-ionic bonding

nature. The materials are mechanically stable and inherently ductile, standing out for their high resistance to compression and superior thermal stability, making them suitable for high-temperature applications. The optical conductivity and absorption spectra exhibit notable features extending beyond the visible region, indicating promising potential for applications in ultraviolet (UV) technologies. The negative Helmholtz free energy values across a wide temperature range (0–1000 K) confirm that these compositions remain thermodynamically stable under varying thermal conditions, indicating a promising candidate for high temperature applications. Overall, Rb_2InAgF_6 is identified as a promising candidate for charge transport devices due to its pronounced density of states features, while the entire family offers a non-toxic, efficient, and robust platform for the development of future clean energy technologies.

Ethical statement

This article does not contain any studies with human participants performed by any of the authors.

Author contributions

Sharmin Islam: investigation, methodology, data curation, writing – original draft. Shatha A. Aldaghfag, Ali El-Rayyes, Abdullah Al Mahmud, Samah Saidi, Omar Alsalmi, Mohd Taukeer Khan: formal analysis, reviewing and editing. Md Saiduzzaman: formal analysis, conceptualization, supervision, writing – original draft, reviewing and editing.

Conflicts of interest

The authors declare that they have no known competing financial interests or personal relationships that could have appeared to influence the work reported in this paper.

Data availability

Data will be made available on request.

Supplementary information (SI): Fig. S1: phonon dispersion spectra of A_2InAgF_6 (A = Na, K, and Rb) compounds. See DOI: https://doi.org/10.1039/d6ra01318j.

Acknowledgements

The authors express their gratitude to Princess Nourah bint Abdulrahman University Researchers Supporting Project number (PNURSP2026R81), Princess Nourah bint Abdulrahman University, Riyadh, Saudi Arabia. The authors extend their appreciation to Northern Border University, Saudi Arabia, for supporting this work through project number (NBU-CRP-2026-2985). This study is supported *via* funding from Prince Sattam bin Abdulaziz University project number (PSAU/2026/R/1447). The researchers wish to extend their sincere gratitude to the Deanship of Scientific Research at the Islamic University of Madinah (KSA) for the support provided to the Post-Publishing Program.

References

1 X.-F. Chen, Periodic Density Functional Theory (PDFT) Simulating Crystal Structures with Microporous CHA Framework: An Accuracy and Efficiency Study, *Inorganics*, 2023, **11**(5), 215, DOI: 10.3390/inorganics11050215.
2 D. Wang, X.-X. Wang, M. L. Jin, P. He and S. Zhang, Molecular level manipulation of charge density for solid-liquid TENG system by proton irradiation, *Nano Energy*, 2022, **103**, 107819, DOI: 10.1016/j.nanoen.2022.107819.
3 H. Zhang, X. Ji, H. Yao, Q. Fan, B. Yu and J. Li, Review on efficiency improvement effort of perovskite solar cell, *Sol. Energy*, 2022, **233**, 421–434, DOI: 10.1016/j.solener.2022.01.060.
4 M. Bošnjaković, Advance of Sustainable Energy Materials: Technology Trends for Silicon-Based Photovoltaic Cells, *Sustainability*, 2024, **16**(18), 7962, DOI: 10.3390/su16187962.
5 C. Ballif, F.-J. Haug, M. Boccard, P. J. Verlinden and G. Hahn, Status and perspectives of crystalline silicon photovoltaics in research and industry, *Nat. Rev. Mater.*, 2022, **7**(8), 597–616, DOI: 10.1038/s41578-022-00423-2.
6 T. S. Ahmad, *et al.*, Optoelectronic and thermoelectric analysis of halide stable double perovskite Rb2TlSbX6 (X = Cl, Br, I) via DFT calculations, *Results Phys.*, 2024, **63**, 107885, DOI: 10.1016/j.rinp.2024.107885.
7 M. S. Uddin, *et al.*, An In-Depth Investigation of the Combined Optoelectronic and Photovoltaic Properties of Lead-Free Cs_2 $AgBiBr_6$ Double Perovskite Solar Cells Using DFT and SCAPS-1D Frameworks, *Adv. Electron. Mater.*, 2024, **10**(5), 2300751, DOI: 10.1002/aelm.202300751.
8 L. Zhang, *et al.*, Advances in the Application of Perovskite Materials, *Nano-Micro Lett.*, 2023, **15**(1), 177, DOI: 10.1007/s40820-023-01140-3.
9 M. Karouchi, *et al.*, Investigating the structural, electronic, and optical properties of the novel double perovskite K2AgBiI6 using DFT, *Front. Mater.*, 2024, **11**, 1448400, DOI: 10.3389/fmats.2024.1448400.
10 Y. Chrafih, M. Al-Hattab and K. Rahmani, Thermodynamic, optical, and morphological studies of the Cs2AgBiX6 double perovskites (X = Cl, Br, and I): Insights from DFT study, *J. Alloys Compd.*, 2023, **960**, 170650, DOI: 10.1016/j.jallcom.2023.170650.
11 E. K. Rugut, N. E. Maluta, R. R. Maphanga, R. E. Mapasha and J. K. Kirui, A Density Functional Theory Insight into Structural, Mechanical, and Optical Properties of Rb_2 $LiTlF_6$ Double Perovskite, *Adv. Eng. Mater.*, 2024, **26**(5), 2300995, DOI: 10.1002/adem.202300995.
12 A. Ayyaz, *et al.*, Structural, morphological, elastic, optoelectronic and thermoelectric properties of lead-free double perovskite Na2AgBiBr6 for photovoltaic applications: Experimental and DFT insight, *Ceram. Int.*, 2024, **50**(9), 15261–15272, DOI: 10.1016/j.ceramint.2024.02.002.
13 A. J. Kale, R. Chaurasiya and A. Dixit, Lead-Free Cs_2 BB′X_6 (B: Ag/Au/Cu, B′: Bi/Sb/Tl, and X: Br/Cl/I) Double Perovskites and Their Potential in Energy Conversion Applications,

ACS Appl. Energy Mater., 2022, **5**(9), 10427–10445, DOI: 10.1021/acsaem.2c00672.

14 S. Bibi, *et al.*, Insight into the physical properties of Rb_2YCuX_6 (X = Br and I) lead-free elpasolite for high-energy applications, *Phys. Scr.*, 2024, **99**(3), 035906, DOI: 10.1088/1402-4896/ad1c81.

15 E. T. McClure, M. R. Ball, W. Windl and P. M. Woodward, Cs_2AgBiX_6 (X = Br, Cl): New Visible Light Absorbing, Lead-Free Halide Perovskite Semiconductors, *Chem. Mater.*, 2016, **28**(5), 1348–1354, DOI: 10.1021/acs.chemmater.5b04231.

16 S. Gupta, J. Kaur, R. Basu, A. K. Sharma, R. Pandey and J. Madan, Lead-free Cs2TiBr6 perovskite solar cells achieving high power conversion efficiency through device simulation, *Micro Nanostruct.*, 2024, **196**, 207991, DOI: 10.1016/j.micrna.2024.207991.

17 M. Tariq, M. A. Ali, A. Laref and G. Murtaza, Anion replacement effect on the physical properties of metal halide double perovskites Cs2AgInX6 (X=F, Cl, Br, I), *Solid State Commun.*, 2020, **314–315**, 113929, DOI: 10.1016/j.ssc.2020.113929.

18 H.-X. Gao, *et al.*, First-principles study on the structural, electronic, elastic, optical and thermodynamic properties of double antiperovskites X6BiSbN2 (X = Mg, Ca, Sr), *J. Phys. Chem. Solids*, 2024, **187**, 111859, DOI: 10.1016/j.jpcs.2023.111859.

19 A. Nazir, A. Dixit, E. A. Khera, M. Manzoor, R. Sharma and A. J. A. Moayad, A DFT exploration of the optoelectronic and thermoelectric features of a novel halide double perovskite A_2YAuI_6 (A = Rb, Cs) for solar cell and renewable energy applications, *Mater. Adv.*, 2024, **5**(10), 4262–4275, DOI: 10.1039/D4MA00090K.

20 Q. Mahmood, *et al.*, Study of lead-free double perovskites X2AgBiI6 (X = K, Rb, Cs) for solar cells and thermoelectric applications, *J. Mater. Res. Technol.*, 2023, **22**, 913–922, DOI: 10.1016/j.jmrt.2022.11.132.

21 N. Rahman, *et al.*, Insight into the structural, mechanical, electronic and optical properties of X2CuAsF6 (X = Na, K) double perovskites for high energy applications employing DFT, *Inorg. Chem. Commun.*, 2024, **166**, 112625, DOI: 10.1016/j.inoche.2024.112625.

22 J. Munir, *et al.*, First-Principles Scrutiny of Double Perovskite Halides A2AlAuCl6 (A = Cs, K, Rb): Potential Contenders for Renewable Energy, *Arabian J. Sci. Eng.*, 2025, **50**(9), 6511–6522, DOI: 10.1007/s13369-024-09462-z.

23 A. U. Haq, *et al.*, A first principle investigation of electronic, mechanical, optical and transport properties of A_2AgAlI_6 (A = Rb, K, Na) for energy harvesting, *Phys. Scr.*, 2023, **98**(11), 115972, DOI: 10.1088/1402-4896/ad032c.

24 T. Lantri, *et al.*, Ab initio exploration of A2AlAgCl6 (A = Rb, Cs): unveiling potentials for UV optoelectronic applications, *J. Mol. Model.*, 2024, **30**(6), 195, DOI: 10.1007/s00894-024-05980-7.

25 N. Israr, A. A. Alothman, S. Mohammad, S. Khan, G. Murtaza and M. Saeed, A2AlInI6 (A = K, Rb, Cs) Double Perovskite Halides for Renewable Energy Applications: A DFT Study on Stability, Light Absorption, and Thermoelectric Performance, *J. Inorg. Organomet. Polym. Mater.*, 2025, **35**(7), 5965–5980, DOI: 10.1007/s10904-025-03634-6.

26 A. B. Siad, H. Riane, M. B. Siad, F. Z. Dahou, A. Allouche and M. Baira, Elevating energy device potential: exploring optoelectronic and thermoelectric advantages in stable double perovskites K2NaInX6 (X = F, Cl, Br, I) via Ab initio analysis, *J. Mater. Sci.*, 2024, **59**(5), 1989–2007, DOI: 10.1007/s10853-023-09229-1.

27 M. A. Ali, A. A. Alothman, M. Mushab, A. Khan and M. Faizan, DFT Insight into Structural, Electronic, Optical and Thermoelectric Properties of Eco-Friendly Double Perovskites Rb2GeSnX6 (X = Cl, Br) for Green Energy Generation, *J. Inorg. Organomet. Polym. Mater.*, 2023, **33**(11), 3402–3412, DOI: 10.1007/s10904-023-02777-8.

28 S. H. Shah, *et al.*, Comprehensive study of structural, elastic, electronic, optical, and thermoelectric properties of Rb2NaTlZ6 (Z = Cl, Br, and I) by DFT, *Mater. Sci. Semicond. Process.*, 2024, **178**, 108400, DOI: 10.1016/j.mssp.2024.108400.

29 S. Shakeel, *et al.*, DFT analysis of elastic and optoelectronic properties of Cs2NaXCl6 (X=In, La, Sc, Y) double perovskite compounds, *Mater. Chem. Phys.*, 2024, **324**(Sep), 129683, DOI: 10.1016/j.matchemphys.2024.129683.

30 S. H. Shah, P. Song, T. Huang, S. Shakeel, S. Khan and G. Murtaza, A pressure tunable optical and thermoelectric properties of Rb2CuSbX6 (X = cl, Br, and I) by FPLAPW+lo method, *Comput. Condens. Matter*, 2024, **39**, e00908, DOI: 10.1016/j.cocom.2024.e00908.

31 S. H. Shah, *et al.*, Uniaxial Strain Engineering of Electronic, Elastic and Optical Properties of Halide Double Perovskites K2NaTIX6 (X = I, Br, and Cl): A DFT Insight, *J. Inorg. Organomet. Polym. Mater.*, 2025, **35**(5), 3665–3681, DOI: 10.1007/s10904-024-03484-8.

32 M. Saeed, *et al.*, Optical and transport properties of novel X2BAgCl6 (where X = K, Rb, Cs, and B = Sc, Y) double perovskites, *Mater. Sci. Eng., B*, 2024, **308**, 117556, DOI: 10.1016/j.mseb.2024.117556.

33 P. Hohenberg and W. Kohn, Inhomogeneous Electron Gas, *Phys. Rev.*, 1964, **136**(3B), B864–B871, DOI: 10.1103/PhysRev.136.B864.

34 W. Kohn and L. J. Sham, Self-Consistent Equations Including Exchange and Correlation Effects, *Phys. Rev.*, 1965, **140**(4A), A1133–A1138, DOI: 10.1103/PhysRev.140.A1133.

35 S. J. Clark, *et al.*, First principles methods using CASTEP, *Z. Kristallogr. Cryst. Mater.*, 2005, **220**(5–6), 567–570, DOI: 10.1524/zkri.220.5.567.65075.

36 J. P. Perdew, K. Burke and M. Ernzerhof, Generalized Gradient Approximation Made Simple, *Phys. Rev. Lett.*, 1996, **77**(18), 3865–3868, DOI: 10.1103/PhysRevLett.77.3865.

37 C. G. BROYDEN, The Convergence of a Class of Double-rank Minimization Algorithms 1. General Considerations, *IMA J. Appl. Math.*, 1970, **6**(1), 76–90, DOI: 10.1093/imamat/6.1.76.

38 R. Fletcher, A new approach to variable metric algorithms, *Comput. J.*, 1970, **13**(3), 317–322, DOI: 10.1093/comjnl/13.3.317.

39 D. Goldfarb, A family of variable-metric methods derived by variational means, *Math. Comput.*, 1970, **24**(109), 23–26, DOI: 10.1090/S0025-5718-1970-0258249-6.

40 D. F. Shanno, Conditioning of quasi-Newton methods for function minimization, *Math. Comput.*, 1970, **24**(111), 647–656, DOI: 10.1090/S0025-5718-1970-0274029-X.

41 S. D. Dipta, J. Islam, S. Gouadria, M. S. Ahmad, A. El-Rayyes and M. Saiduzzaman, First-principles investigation of lead-free double perovskites Cs_2 $NaGaX_6$ (X = F, Cl, and Br) for optoelectronic applications, *New J. Chem.*, 2026, **50**(11), 4910–4928, DOI: 10.1039/D5NJ04533A.

42 M. Shakil, *et al.*, Computational investigation of newly proposed double halide perovskites Cs2GaBiX6 (X = Cl, Br and I) with enhanced optoelectronic properties for green energy harvesting and photocatalytic applications, *J. Phys. Chem. Solids*, 2025, **201**, 112638, DOI: 10.1016/j.jpcs.2025.112638.

43 K.-E. Peiponen, V. Lucarini, E. M. Vartiainen and J. J. Saarinen, Kramers-Kronig relations and sum rules of negative refractive index media, *Eur. Phys. J. B.*, 2004, **41**(1), 61–65, DOI: 10.1140/epjb/e2004-00294-6.

44 K. Momma and F. Izumi, *VESTA 3* for three-dimensional visualization of crystal, volumetric and morphology data, *J. Appl. Crystallogr.*, 2011, **44**(6), 1272–1276, DOI: 10.1107/S0021889811038970.

45 R. Gaillac, P. Pullumbi and F.-X. Coudert, ELATE: an open-source online application for analysis and visualization of elastic tensors, *J. Phys. Condens. Matter*, 2016, **28**(27), 275201, DOI: 10.1088/0953-8984/28/27/275201.

46 C. J. Bartel, A. Trewartha, Q. Wang, A. Dunn, A. Jain and G. Ceder, A critical examination of compound stability predictions from machine-learned formation energies, *npj Comput. Mater.*, 2020, **6**(1), 97, DOI: 10.1038/s41524-020-00362-y.

47 N. Laihnuna, *et al.*, Multifaceted analysis of K2InAgX6 (X = F, Cl, Br, I) for photovoltaic and thermoelectric applications, *J. Phys. Chem. Solids*, 2024, **195**, 112291, DOI: 10.1016/j.jpcs.2024.112291.

48 S. Ahmad, *et al.*, DFT study of elastic, structural, and optical properties of K2InAgZ6 (Z = Cl, Br, I) perovskites: potential for optoelectronic applications, *Opt. Quant. Electron.*, 2024, **56**(12), 1946, DOI: 10.1007/s11082-024-07769-7.

49 A. Cheng, C. Lyu, T. Shi, Z. Wang and R. Palgrave, *Geometric Analysis and Formability of the Cubic A2BX6 Vacancy Ordered Double Perovskite Structure*, Jul. 03, 2020, DOI: 10.26434/chemrxiv.12601538.v1.

50 S. Jamshaid, *et al.*, Investigation of cubic K2NaXBr6(X=Sc, Y) double perovskites for optical and thermoelectric devices, *J. Phys. Chem. Solids*, 2023, **178**, 111341, DOI: 10.1016/j.jpcs.2023.111341.

51 Y. Fu, *et al.*, Incorporating Large A Cations into Lead Iodide Perovskite Cages: Relaxed Goldschmidt Tolerance Factor and Impact on Exciton–Phonon Interaction, *ACS Cent. Sci.*, 2019, **5**(8), 1377–1386, DOI: 10.1021/acscentsci.9b00367.

52 C. J. Bartel, *et al.*, New tolerance factor to predict the stability of perovskite oxides and halides, *Sci. Adv.*, 2019, **5**(2), eaav0693, DOI: 10.1126/sciadv.aav0693.

53 Z. B. Wang, B. S. Luk'yanchuk, M. H. Hong, Y. Lin and T. C. Chong, Energy flow around a small particle investigated by classical Mie theory, *Phys. Rev. B: Condens. Matter Mater. Phys.*, 2004, **70**(3), 035418, DOI: 10.1103/PhysRevB.70.035418.

54 I. Waller, Dynamical theory of crystal lattices by M. Born and K. Huang, *Acta Crystallogr.*, 1956, **9**(10), 837–838.

55 L. W. Finger, Physical Properties of Crystals, Their Representation by Tensors and Matrices, *EOS Trans. Am. Geophys. Union*, 1983, **64**(45), 643, DOI: 10.1029/EO064i045p00643-01.

56 C. Kittel and P. McEuen, *Introduction to Solid State Physics*, John Wiley & Sons, 2018.

57 F. Mouhat and F.-X. Coudert, Necessary and sufficient elastic stability conditions in various crystal systems, *Phys. Rev. B: Condens. Matter Mater. Phys.*, 2014, **90**(22), 224104, DOI: 10.1103/PhysRevB.90.224104.

58 I. A. Ovi, M. R. Hasan, I. A. Apon and F.-T. Zahra, The structural, magnetic, optoelectronic, and mechanical characteristics of NaGeX3 perovskites under pressure for soler-cell applications, *Mater. Res. Express*, 2024, **11**(6), 065904, DOI: 10.1088/2053-1591/ad594d.

59 N. Coburn, Review of Finite Deformations of an Elastic Solid, *Math. Mag.*, 1953, **27**(2), 109–111, DOI: 10.2307/3029772.

60 T. E. Jones, T. C. R. Rocha, A. Knop-Gericke, C. Stampfl, R. Schlögl and S. Piccinin, Adsorbate induced vacancy formation on silver surfaces, *Phys. Chem. Chem. Phys.*, 2014, **16**(19), 9002–9014, DOI: 10.1039/C4CP00778F.

61 R. Hill, The elastic behaviour of a crystalline aggregate, *Proc. Phys. Soc. London, Sec. A*, 1952, **65**(5), 349.

62 M. Al-Fahdi, A. Rodriguez, T. Ouyang and M. Hu, High-throughput computation of new carbon allotropes with diverse hybridization and ultrahigh hardness, *Crystals*, 2021, **11**(7), 783.

63 Md. A. Hossain, *et al.*, Investigation of the physical properties and pressure-induced band gap tuning of Sr3ZBr3 (Z = As, Sb) for optoelectronic and thermoelectric applications: A DFT - GGA and mBJ studies, *Results Eng.*, 2024, 103340, DOI: 10.1016/j.rineng.2024.103340.

64 G. N. Greaves, A. L. Greer, R. S. Lakes and T. Rouxel, Author Correction: Poisson's ratio and modern materials, *Nat. Mater.*, 2019, **18**(4), 406, DOI: 10.1038/s41563-019-0319-2.

65 M. T. Hossain, T. Akter, J. Islam, M. A.-A. B. Shuvo, K. Hossain and M. A. Hossain, Investigation of structural, mechanical, electronic, optical, and thermodynamic properties of AXI3 (A = Li, Na; X = Ca, Sr, and Ba) halide perovskites for emerging energy technologies: A DFT study, *Mater. Sci. Semicond. Process.*, 2025, **188**, 109235, DOI: 10.1016/j.mssp.2024.109235.

66 G. Feng, Y. Qin, C. Ran, L. Ji, L. Dong and W. Li, Structural evolution and photoluminescence properties of a 2D hybrid perovskite under pressure, *APL Mater.*, 2018, **6**(11), 114201, DOI: 10.1063/1.5042645.

67 Q.-J. Hong, Melting temperature prediction via first principles and deep learning, *Comput. Mater. Sci.*, 2022, **214**, 111684, DOI: 10.1016/j.commatsci.2022.111684.

68 A. Ejjabli, M. Karouchi, M. Al-Hattab, O. Bajjou, K. Rahmani and Y. Lachtioui, Investigation of lead-free halide K2AgSbBr6 double Perovskite's structural, electronic, and optical properties using DFT functionals, *Chem. Phys. Impact*, 2024, **9**, 100656, DOI: 10.1016/j.chphi.2024.100656.

69 N. Israr, A. A. Alothman, S. Mohammad, S. Khan, G. Murtaza and M. Saeed, A2AlInI6 (A = K, Rb, Cs) Double Perovskite Halides for Renewable Energy Applications: A DFT Study on Stability, Light Absorption, and Thermoelectric Performance, *J. Inorg. Organomet. Polym. Mater.*, 2025, **35**(7), 5965–5980, DOI: 10.1007/s10904-025-03634-6.

70 N. A. Noor, *et al.*, Analysis of direct band gap A2ScInI6 (A=Rb, Cs) double perovskite halides using DFT approach for renewable energy devices, *J. Mater. Res. Technol.*, 2021, **13**, 2491–2500, DOI: 10.1016/j.jmrt.2021.05.080.

71 M. Caid, D. Rached, S. Al-Qaisi, Y. Rached and H. Rached, DFT calculations on physical properties of the lead-free halide-based double perovskite compound Cs2CdZnCl6, *Solid State Commun.*, 2023, **369**, 115216, DOI: 10.1016/j.ssc.2023.115216.

72 Md. H. Ali, *et al.*, Investigation of Structural, Electronic and Optical Properties of Na2InAgCl6, K2InAgCl6, and Rb2InAgCl6 Lead-Free Halide Double Perovskites Regarding with Cs2InAgCl6 Perovskites Cell and a Comparative Study by DFT Functionals, *Mater. Res.*, 2021, **24**(6), e20210086, DOI: 10.1590/1980-5373-mr-2021-0086.

73 S. Zuhair Abbas Shah, S. Niaz, T. Nasir and S. M. Ramay, Exploring the structural, phononic, electronic, magnetic, optical, and thermoelectric properties of Pb-free vanadium-based double perovskites using the first-principles approach for optoelectronic and thermoelectric applications, *Sol. Energy*, 2022, **240**, 27–37, DOI: 10.1016/j.solener.2022.05.021.

74 S. Boucetta, Theoretical study of elastic, mechanical and thermodynamic properties of MgRh intermetallic compound, *J. Magnes. Alloys*, 2014, **2**(1), 59–63, DOI: 10.1016/j.jma.2014.04.001.

75 U. Chakma, A. Kumer, K. B. Chakma, M. T. Islam, D. Howlader and R. M. K. Mohamed, Electronics structure and optical properties of SrPbO3 and SrPb0.94Fe0.06O3: A first principle approach, *Eurasian Chem. Commun.*, 2020, **2**(5), 573–580, DOI: 10.33945/SAMI/ECC.2020.5.2.

76 E. F. Schubert, J. K. Kim and J. -Q. Xi, Low-refractive-index materials: A new class of optical thin-film materials, *Phys. Status Solidi B*, 2007, **244**(8), 3002–3008, DOI: 10.1002/pssb.200675603.

77 H. H. Hegazy, G. M. Mustafa, A. Nawaz, N. A. Noor, A. Dahshan and I. Boukhris, Tuning of direct bandgap of Rb2ScTlX6 (X = Cl, Br, I) double perovskites through halide ion substitution for solar cell devices, *J. Mater. Res. Technol.*, 2022, **19**, 1271–1281, DOI: 10.1016/j.jmrt.2022.05.082.

78 R. Yang, D. Li, S. L. Salazar, Z. Rao, M. Arıcı and W. Wei, Photothermal properties and photothermal conversion performance of nano-enhanced paraffin as a phase change thermal energy storage material, *Sol. Energy Mater. Sol. Cells*, 2021, **219**, 110792, DOI: 10.1016/j.solmat.2020.110792.

79 S. H. Shah, *et al.*, DFT investigation on thermoelectric, electronic, optoelectronic, elastic, and structural properties of sodium-based halide double perovskites Rb_2 $NaSbZ_6$ (Z = Cl, Br, and I), *J. Chin. Chem. Soc.*, 2025, **72**(2), 211–228, DOI: 10.1002/jccs.202400254.

80 R. Ali, S. Shakeel, H. Dou and H. E. Wang, Unveiling the hydrogen storage potential of Cs_2LiGaH_6 and Cs_2LiInH_6: A DFT study on novel double perovskite hydrides, *Int. J. Hydrogen Energy*, 2025, **193**(28), 152365.

81 C. Li, H. Hu, C. Xu, H. Xiao, L. Yi, C. Ma, L. Liu and Q. Chen, Atomic occupation of Nb in AB_2-type alloy and its effect on hydrogen storage property, *Rare Met.*, 2025, **44**(12), 10646–10659.

82 Y. X. Zhang, G. J. Wu, J. Gu, H. X. Kang, Y. Li, D. Zhou, W. F. Wang, L. Zhang and S. M. Han, A_2B_7-type La–Mg–Ni alloys prepared by Mg thermal diffusion for improved hydrogen storage performance, *Rare Met.*, 2024, **43**(7), 3260–3272.

83 P. Ghosez, E. Cockayne, U. V. Waghmare and K. M. Rabe, Lattice dynamics of BaTiO3,PbTi3, and PbZrO3: A comparative first-principles study, *Phys. Rev. B: Condens. Matter Mater. Phys.*, 1999, **60**(2), 836–843.

84 W. Su, *et al.*, Synthesis and Stability of Hydrogen Storage Material Aluminum Hydride, *Materials*, 2021, **14**(11), 2898.

85 N. K. Nepal, P. C. Canfield and L. L. Wang, Imaginary phonon modes and phonon-mediated superconductivity in Y2C3, *Phys. Rev. B*, 2024, **109**(5), 054518.

86 X. Wanget al, Dilute carbon in H3S under pressure, *npj Comput. Mater.*, 2022, **8**(1), 87.

87 S. A. Khandy, I. Islam, K. Kaur, A. M. Ali and A. F. A. El-Rehim, Electronic structure, stability, photocatalytic and optical properties of new lead-free double perovskites Tl2PtX6 (X = Cl, Br) for light-harvesting applications, *Mater. Chem. Phys.*, 2023, **297**, 127293, DOI: 10.1016/j.matchemphys.2023.127293.